Nano Research

ISSN 1998-0124 CN 11-5974/O4
https://doi.org/10.1007/s12274-024-6763-6

Review Article

Thermal transports in the MXenes family: Opportunities and challenges

Yurui Liu[1], Yue Wu[1] (✉), and Xinwei Wang[2] (✉)

[1] *Department of Chemical and Biological Engineering, Iowa State University, 618 Bissell Ames, IA 50011, USA*
[2] *Department of Mechanical Engineering, 271 Applied Science Complex II, 1915 Scholl Road, Iowa State University, Ames, IA 50011, USA*

Received: 29 April 2024 / **Revised:** 13 May 2024 / **Accepted:** 13 May 2024

ABSTRACT

The carbides and nitrides of transition metals known as "MXenes" refer to a fast-growing family of two-dimensional materials discovered in 2011. Thanks to their unique nanolayer structure, superior electrical, mechanical, and thermal properties, MXenes have shown great potential in addressing the critical overheating issues that jeopardize the performance, stability, and lifetime of high-energy-density components in modern devices such as microprocessors, integrated circuits, and capacitors, etc. The outstanding intrinsic thermal conductivity of MXenes has been proved by experimental and theoretical research. Numerous MXenes-enabled high thermal conductivity composites incorporated with polymer matrix have also been reported and widely used as thermal management materials. Considering the booming heat dissipation demands, MXenes-enabled thermal management material is an extremely valuable and scalable option for modern electronics industries. However, the fundamental thermal transport mechanisms behind the MXenes family remain unclear. The MXene thermal conductivity disparities between the theoretical prediction and experimental results are still significant. To better understand the thermal conduction in MXenes and provide more insights for engineering high-performance MXene thermal management materials, in this article, we summarize recent progress on thermal conductive MXenes. The essential factors that affect MXenes intrinsic thermal conductivities are tackled, selected MXenes-polymer composites are highlighted, and prospects and challenges are also discussed.

KEYWORDS

transition metal carbide (MXene), thermal transport, two-dimensional materials, thermally conductive composites

1 Introduction

As a class of two-dimensional (2D) material emerged in the last decade, the carbides and nitrides of transition metals known as "MXenes" have attracted significant attention since the discovery in 2011 by Gogotsi and co-workers [1]. Thanks to their superior properties given by the unique 2D nanostructure, MXenes have been considered a promising candidate in broad fields including but not limited to electrical, optical, mechanical, and thermal applications [2–7]. With the intensive integration and miniaturization trend of highly integrated electronics, modern device evolution has constantly approached the boundaries predicted by Moore's law [8]. As the continuously shrinking dimension and rising energy density of devices, the demand for effective heat dissipation rises. Massive thermal energy produced by heat-generating components in microelectronics (e.g., microprocessors, photonic integrated circuits, etc.) can lead to local overheating problems. The improper operating temperature will degrade the performance of electronic components and further decrease the device's lifetime. To date, heat dissipation has become an essential bottleneck in the growth of electronic industries [9–11]. Tremendous research efforts have been devoted to developing thermal-management materials that can satisfy the fast-growing heat dissipation needs of microelectronics [12]. Low-dimensional materials with outstanding intrinsic thermal conductivity shed light on thermal transport in nanoscales and are of fundamental importance for the design of thermal interface materials (TIMs). There have been studies predicted that MXenes, like other representative two-dimensional materials such as graphene (thermal conductivity $\kappa \sim 10^3$ W·m^{-1}·K^{-1}) [13–15], hexagonal boron nitride (thermal conductivity $\kappa \sim 600$ W·m^{-1}·K^{-1}) [16], and transition metal dichalcogenides (TMDs, e.g. thermal conductivity of MoS_2 range from 31 to 110 W·m^{-1}·K^{-1}) [17–21] etc., possesses superior theoretical thermal conductivities. Due to the unique combination of outstanding intrinsic thermal conductivity, mechanical strength, and highly tunable surface chemical properties, MXenes show great potential as next-generation thermal-management materials.

1.1 Rising of the MXenes family

As the name "MXenes" implies, "MX" is derived from the MAX phase, which is the ternary ceramic precursor of MXenes in the commonly used top-down synthesize method, (the general formula of MAX can be written as $M_{n+1}AX_n$, whereas M represents early transition metal, A is the element from groups 12 to 16 of the periodic table, X belongs to carbon or nitrogen) [22], and "enes" suggests that MXenes shares a similar microscopic structure with graphene. Similarly, MXenes can be expressed in the simple general formula $M_{n+1}X_nT_x$ (whereas T stands for the

Address correspondence to Yue Wu, yuewu@iastate.edu; Xinwei Wang, xwang3@iastate.edu

surface termination group such as fluorine, oxygen, and chlorine, and x is the number of surface terminations).

The fast growth of the MXenes family has been witnessed in the past decades since the first MXenes example $Ti_3C_2T_x$ was discovered in 2011 [1]. To date, over 150 MAX precursors and 40 MXenes have been successfully synthesized [23, 24]. MXenes with more diverse stoichiometric compositions and structures have been computationally predicted (Fig. 1) [23, 24]. By varying the n number and M sites elements, higher order MXenes and more unique structures such as solid solution MXenes, in-plane ordered/out-of-plane ordered MXenes and high entropy MXene have been studied [25].

To satisfy different application requirements (such as flake size and thickness, flake topology, type of terminal group, etc.), different synthetic schemes of MXene have been explored. The earliest synthesis of MXene starts from selectively etching the "A" element in the MAX phase (for example, Ti_3AlC_2) via hydrofluoric acid (HF) resulting in multi-layered MXene flakes packed by hydrogen bond and van der Waals (VDWs) force [1]. To further delaminate multi-layered MXenes, the sonification process and intercalants are induced to weaken the interactions between MXene layers in the top-down synthesis route of MXenes. The development of the LiF-HCl etching method by *in situ* mixing lithium fluoride (LiF) and hydrochloric acid (HCl) further eliminates the dangers of using HF in MXenes preparation and provides a more environmentally green route. This *in situ* etching route has also been modified into the minimally intensive layer delamination (MILD) method that achieved the synthesis of single and larger MXenes flakes without the sonification process [26–29]. Thanks to the milder delaminating condition, the MILD method produced $Ti_3C_2T_x$ flakes have been proved with fewer surface defects and shown corresponding grain size/shape with MAX precursor [28]. Moreover, the bottom-up approaches for MXene materials growth can realize atomic scale controlled synthesis [30]. Mo_2C films prepared by chemical vapor deposition (CVD) and plasma-enhanced pulsed laser deposition (PELPD) techniques have been reported [31, 32]. Though stemming from the inherent technique limitation, MXene materials based on the bottom-up method are far from scalable synthesis and application, the bottom-up approach prepared MXenes possesses merits such as defect-free and highly crystalline, which are valuable for basic research including thermal transport.

The diversity of material dimensionality further extends the range of the MXenes family and has attracted extensive research interest. The first reported $Ti_3C_2T_x$ nanosheets exhibit typical 2D material characteristics [1]. Zero-dimensional (0D) MXenes quantum dots (MQDs) synthesized by the hydrothermal method were reported in 2017, and rational control of MQDs morphology and size distribution has also been investigated [33]. MXene nanoribbons (MNRs) that are considered as quasi-one-dimensional (1D) materials were predicted in 2015 [34]. Succeed fabrication of MNRs was realized later in 2017 [35]. Three-dimensional (3D) MXene networks constructed by template-assistant method [36], freeze-drying method [37, 38], etc., have also been extensively studied. Thanks to the diversity and unique nature of MXenes, this fast-expanding family has irreplaceable advantages in the field of thermal transport. So far, advanced progress in MXene thermal transport has gained tremendous attention, and the underlying heat transfer mechanisms are desired to be unveiled.

1.2 Fundamental mechanisms in MXenes thermal transport

Considering the highly crystalline structure and metallic electrical properties in MXenes, both electrons and phonons are heat carriers, and the thermal conductivity can be decomposed into the electron motions (κ_e) and lattice vibration (κ_l) portion. The proportionality between electron-contributed thermal conductivity (κ_e) and electrical conductivity is described by the Wiedemann-Franz law in the Eq. (1) [39]

$$\kappa_e = L_0 \sigma_e T \tag{1}$$

whereas σ_e is electrical conductivity, L_0 is the Lorentz number, and T is the absolute temperature. Thanks to the periodicity of MXene structure, the quantized vibration modes of lattice (phonon) are well-defined in MXenes. Phonons contribute to lattice thermal conductivity κ_l, numerous thermal transport models in crystalline solids have been well established. Among them, the kinetic theory

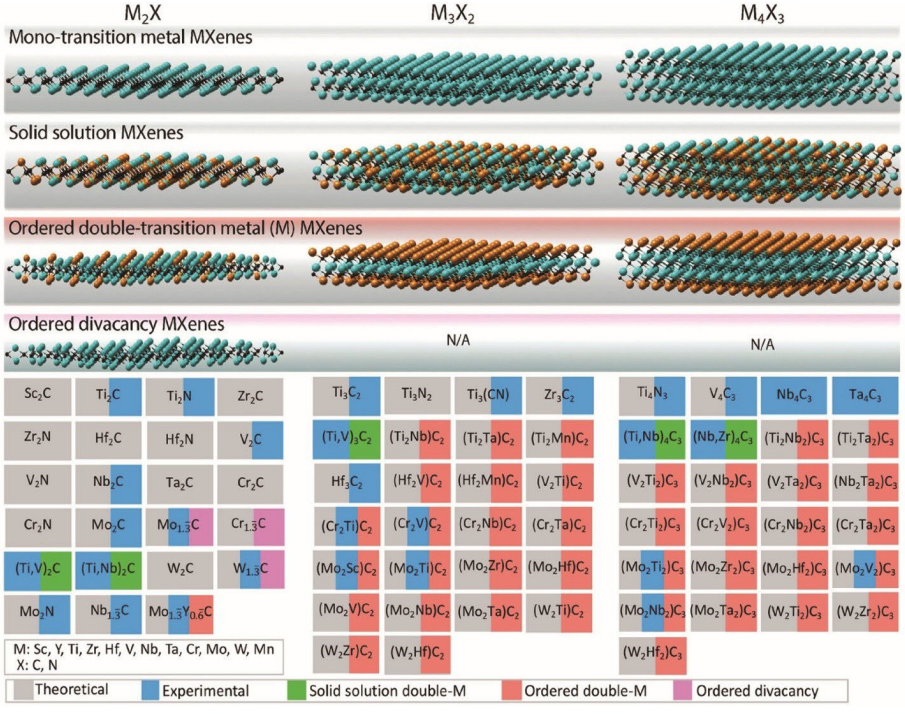

Figure 1 MXenes family overview and classification, reproduced with permission from Ref. [23], © American Chemical Society 2019.

of gas (Eq. (2)) laid a fundamental picture of phonon-enabled thermal transport in crystals [40, 41].

$$\kappa_l = \sum_{\omega} c_{(\omega)} v_{(\omega)} \Lambda_{(\omega)} \quad (2)$$

whereas ω denotes the phonon mode in the phonon branch with angular frequency ω, $c_{(\omega)}$ is the frequency-dependent heat capacity and can be expressed as $c_{(\omega)} = \hbar\omega \frac{\partial f_\lambda^0}{\partial T}$, f_λ^0 is the equilibrium phonon distribution function obey the Bose-Einstein statistics, $\hbar$ is the reduced Planck's constant, and T is the absolute temperature. $v_{(\omega)}$ is the phonon group velocity defined as $v_{(\omega)} = \frac{\partial \omega}{\partial k}$ (k is wavenumber). $\Lambda_{(\omega)}$ is the phonon mean free path (the average distance that a phonon particle travels before each collision). Kinetic theory of gas based on relaxation time approximation and Debye approximation can be written as an integration over the phonon spectrum, considering the Van der Waals force induced interlayer interaction between 2D MXene flakes, the generalized expression of by Eq. (3)

$$\kappa_l = \frac{1}{2}\int c_{(\omega)} v_{(\omega)} \Lambda_{(\omega)} \mathrm{d}\omega = \frac{1}{2}\int c_{(\omega)} v_{(\omega)}^2 \tau_{(\omega)} \mathrm{d}\omega \quad (3)$$

whereas $\tau_{(\omega)}$ is the phonon relaxation time defined as $\tau_{(\omega)} = \frac{\Lambda_{(\omega)}}{V_{(\omega)}}$. The phonon relaxation time τ is induced to describe the effect of all possible scattering mechanisms and can be estimated by Matthiessen's rule (Eq. (4)) [42]

$$\frac{1}{\tau} = \sum_k \frac{1}{\tau_k} \quad (4)$$

whereas k represents different scattering approaches such as phonon-phonon scattering (τ_{PP}), impurity scattering (τ_I), and boundary scattering (τ_B), etc. All possible scattering mechanisms are assumed to be independent of each other. In highly crystalline solids, the phonon mean free path ranges from the inter-atomic spaces to the crystal size [43]. As the characteristic size (d) of nanocrystals (flake thickness in the case of 2D materials) becomes comparable or smaller than the effective phonon mean free path ($(1/\Lambda_{elastic} + 1/\Lambda_{inelastic})^{-1}$), the diffusion approximation in classic macroscope thermal transport theory (Fourier's law) is no longer valid, heat conduction fall into the classical size effect regime, phonon motion undergoes a transition from diffusion transport to ballistic transport [39, 43, 44]. Size and interface effects become pronounced along with the crossover from diffusive regime to ballistic regime.

The linearized phonon Boltzmann transport equation (BTE) can be applied to both ballistic and diffusive transport regimes as shown in Eq. (5) [42, 45, 46]

$$\kappa_l^{\alpha\beta} = \frac{1}{k_B T^2 N V} \sum_\lambda f_\lambda^0 (f_\lambda^0 + 1) (\hbar\omega_\lambda)^2 v_\lambda^\alpha F_\lambda^\beta \quad (5)$$

whereas k_B, T, $\hbar$, V, and N are the Boltzmann constant, absolute temperature, reduced Planck's constant, the volume of the unit cell, and the number of points used to sample the q space, respectively. The different phonon mode is denoted as λ, f_λ^0 is the equilibrium phonon distribution function obeying the Bose-Einstein statistics, ω_λ is the angular frequency, v_λ is the group velocity and F_λ is the mean free displacement. The BTE model provided a bridge between ballistic and diffusive models, and lattice thermal conductivity modeling in MXenes based on BTE is widely accepted [45, 46].

Klemens' theory considers the influence induced by various types of defects and impurities can be written as Eq. (6) [47, 48]. This approximation expression integrated the simplified phonon dispersion relations (for example, the Debye model) and coefficient of different phonon branches determined by quantitatively fitting their experiment result [49]. Klemens model is now extensively used in MXene thermal behavior simulation. Theoretical predicted thermal transport properties of Hf_2CO_2, Ti_2CO_2, Zr_2CO_2, Mo_2C, Sc_2CT_2, etc., based on Klemens theory have been reported [50–52].

$$\kappa_l = \sum_j \frac{\rho}{<\gamma_j^2>} \frac{<v_j>^4}{\omega_{\max,j} T} \ln \frac{\omega_{\max,j}}{\omega_{\min,j}} \quad (6)$$

whereas ρ is mass density, and calculated by $\rho = \frac{M}{\left(\frac{\sqrt{3}}{2} a^2 d\right)}$, ($M$ is the mass of the unit cell, a and d denoting the hexagonal lattice parameter), v_j, γ_j, $\omega_{\max,j}$ and $\omega_{\min,j}$ are the group velocity, Grüneisen parameter, the minimum and maximum circular frequency, of the j-branch in phonon spectrum, respectively.

Theoretically, low-dimension systems including MXenes might not necessarily converge to constant thermal conductivity value even with a large enough system scale due to the lack of scattering mechanisms [53]. Diverging thermal conductivity could be due to potential hydrodynamic and/or coherent transport. Hydrodynamic transport occurs as the boundary scattering process dominates over the Umklapp scattering (which the thermal resistance origins from) and is weaker compared with the normal scattering process ($\gamma_{normal} > v_g/d > \gamma_{Umklapp}$), whereas v_g is phonon group velocity and d is the sample characteristic size). In the hydrodynamic regime, phonons exhibit macroscopic drift motion, heat pulse propagates as phonon population wave (known as second sound) potentially contributing to the more efficient pathway of thermal transport [49, 54]. Stemming from the dimensionality confinement of 2D materials, hydrodynamic phono transports have already been investigated in other 2D materials such as graphene, boron nitride, etc. [55, 56]. Coherent phonon transport can be observed as the characteristic size of system d becomes comparable to or shorter than the coherent length of heat carriers. One extreme case of coherent thermal transport is the Fermi–Pasta–Ulam (FPU) theory which suggests a potential divergent thermal conductivity [57]. However, the coherent transport phenomenon is only significant in perfect lattice or low temperature due to strong materials/temperature dependent on phonon coherent length [58], and the broadband wave nature of the phonon spectrum (from ~ 100 GHz to ~ 10 THz) [49]. To the best of our knowledge, the hydrodynamic transport in MXene materials has not been experimentally confirmed. Theoretical prediction of MXene thermal conductivity shows promising thermal transport capability but also considerable variability. MXenes with highly tunable sites, various compositions, and alternating layers structures at the atomic level exhibited great potential in phononic engineering and are regarded as promising thermal conductor candidates [12, 49].

2 Advances in MXenes thermal properties studies

To date, significant efforts have been made in the investigation of the thermal properties of the MXenes family. Theoretical predicted thermal conductivities of MXenes range from tens to hundreds of $W \cdot m^{-1} \cdot K^{-1}$ [45, 46, 50–52, 59–62, 67], which show a considerable discrepancy with the experimental results (Fig. 2) [64]. The detailed investigations of phonon transport behavior in the fast-growing MXenes family still lack, a fundamental understanding of thermal transport mechanisms behind MXene remains unclear, and in-depth studies in the related area are highly desired. To better understand the structure-property relationships

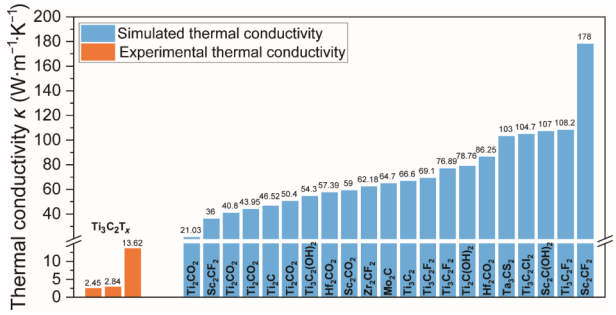

Figure 2 Current gap between the reported simulated [45, 46, 50–52, 59–62] and experimental [63–66] results of MXenes thermal conductivity.

in MXenes thermal transport and unveil details for mechanistic studies, we summarized the elements that affect MXene thermal transport including the hot carriers' contribution [59, 62–65, 68], anisotropic thermal conductivities [51, 52, 59], size effect [50, 52], surface functional groups effect, etc. [45, 46, 59–61]. The representative thermal conductivity simulation results of MXenes are summarized in Table 1.

2.1 Effect of hot carriers' contribution to MXenes thermal conductivity

Non-terminated (bare) MXenes are commonly known to be metallic, and several fluorine (–F) and (–OH) hydroxyl-terminated MXenes with larger bandgap have been reported as semiconductors. This leads to a disagreement about the dominant hot carriers in MXenes. Both electron and phonon (quantum of lattice vibrational energy) dominate the thermal transport in metallic solids, while in the case of semiconductors, phonon plays the dominant hot carrier role [68]. To further clarify the nanoscale thermal transport mechanism behind MXenes, it is of fundamental importance to investigate the contribution of hot carriers. In 2018, Guo et al. calculated both the electron conductivity and phonon conductivity of Ti_2CT_2 (whereas T = –OH, –F, and –O) [59]. The results suggest that though the non-terminated Ti_2C exhibited metallic electrical conductivity, the predicted electron thermal conductivity is exceeded by its phonon counterpart (κ_e ~ 20 $W{\cdot}m^{-1}{\cdot}K^{-1}$ and κ_l ~ 46.52 $W{\cdot}m^{-1}{\cdot}K^{-1}$/65.20 $W{\cdot}m^{-1}{\cdot}K^{-1}$ along the zigzag direction and the armchair direction, respectively), further investigation suggests that different terminal group will also affect both the electron and phonon thermal

Table 1 Selected theoretical thermal conductivity of the MXenes family at room temperature [45, 46, 50–52, 59–62]

MXene	Thermal conductivity κ ($W{\cdot}m^{-1}{\cdot}K^{-1}$)	Years	Ref.
Mo_2C	64.7 (along the zigzag direction) 48.4 (along the armchair direction)	2016	[51]
Hf_2CO_2	86.25 (along the armchair direction)	2016	[50]
Zr_2CO_2	62.18 (along the armchair direction)	2016	[50]
Ti_2CO_2	21.03 (along the armchair direction)	2016	[50]
Sc_2CF_2	178 (along the zigzag direction) 472 (along the armchair direction)	2016	[52]
$Sc_2C(OH)_2$	107 (along the zigzag direction) 173 (along the armchair direction)	2016	[52]
Sc_2CO_2	59	2016	[45]
Sc_2CF_2	36	2016	[45]
$Sc_2C(OH)_2$	10	2016	[45]
Ti_2C	46.52 (along the zigzag direction) 65.20 (along the armchair direction)	2018	[59]
Ti_2CO_2	43.95 (along the zigzag direction) 53.30 (along the armchair direction)	2018	[59]
Ti_2CF_2	76.89 (along the zigzag direction) 82.49 (along the armchair direction)	2018	[59]
$Ti_2C(OH)_2$	78.76 (along the zigzag direction) 109.95 (along the armchair direction)	2018	[59]
Ti_2CO_2	40.8 (MD-II)-18.42 (MD-III)	2018	[60]
Zr_2CO_2	50.40 (MD-II)-16.85 (MD-III)	2018	[60]
Hf_2CO_2	57.39 (MD-II)-27.43 (MD-III)	2018	[60]
Sc_2CO_2	Metal (MD-II)- 47.01 (MD-III)	2018	[60]
Ti_3C_2	66.6	2019	[61]
$Ti_3C_2F_2$	108.2	2019	[61]
$Ti_3C_2O_2$	11.19	2019	[61]
Ta_2CS_2	103 (asymmetric) 13 (symmetric)	2022	[46]
$Ti_3C_2F_2$	69.1	2022	[62]
$Ti_3C_2Cl_2$	104.7	2022	[62]
$Ti_3C_2(OH)_2$	54.3	2022	[62]

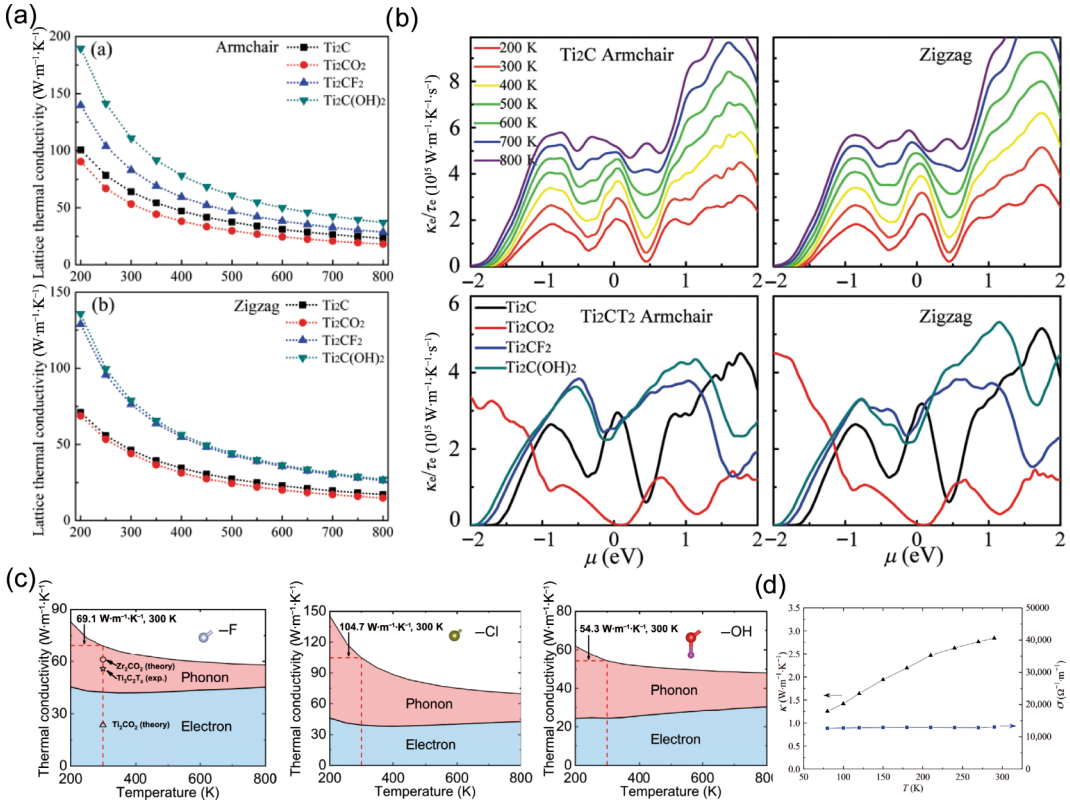

Figure 3 (a) Temperature-dependent lattice thermal conductivity of Ti_2CT_2 along armchair and zigzag direction. Reproduced with permission from Ref. [59], © Royal Society of Chemistry 2018. (b) Chemical potential dependent-electron thermal conductivity of Ti_2CT_2 with fixed electron relaxation time along armchair and zigzag direction. Reproduced with permission from Ref. [59], © Royal Society of Chemistry 2018. (c) Temperature-dependent lattice and electron thermal conductivity contribution in Ti_2CT_2. Reproduced with permission from Ref. [62], © American Physical Society 2022. (d) Temperature-dependent lattice and electron thermal conductivity contribution in $Ti_3C_2T_x$ film. Reproduced with permission from Ref. [65], © Chen, L. et al. 2018.

conductivity. Figure 3(a) shows the anisotropic phonon thermal conductivity κ_l at armchair and zigzag direction. Figure 3(b) shows the electron thermal conductivity κ_e with constant electron relaxation time τ_e at different chemical potentials μ, simulated results suggest that the electron thermal conductivity is in-plane anisotropic [59]. Recently, Wang et al. further studied the role of electrons on the thermal conductivity of typical metallic Ti_2CT_2 (whereas T = –F, –Cl, and –OH) [62]. The overall thermal conductivity of these three MXenes ranged from 54.3 to 104.7 $W \cdot m^{-1} \cdot K^{-1}$ around room temperature, the electrons contributed to 37.3%–61.3% of the total thermal conductivity (Fig. 3(c)) [62]. The acoustic phonons are found to be the main contributor to lattice thermal conductivity, their lifetime is severely restricted by the strong phonon-electron scattering [62]. However, the experimental results of MXene thermal transport behavior on macroscopic scale showed considerable discrepancy from the simulated data described above [65]. Chen et al. measured the thermal conductivity value of filtrated $Ti_3C_2T_x$ film by the Steady-state T-type method (Table 2) and exhibited room temperature thermal conductivity ~ 2.84 $W \cdot m^{-1} \cdot K^{-1}$ [65]. This result is significantly lower than previous predictions of $Ti_3C_2T_x$ [61, 62]. Chen et al. also revealed the thermal conductivity and electrical conductivity temperature dependence of the filtrated $Ti_3C_2T_x$ film from 80 to 290 K (Fig. 3(d)). The electrical conductivity of $Ti_3C_2T_x$ film remains stable at 12,800 $\Omega^{-1} \cdot m^{-1}$ in the temperature range. According to the Wiedemann-Franz law, the electron contribution (κ_e) to the measured thermal conductivity only accounts for 3.26% [65], recent reported experimental results from Wu and Yu et al. also suggest that electron contribution to the total thermal transport in $Ti_3C_2T_x$ is less than 1%, which is surprisingly low [63, 64]. Considering the inter-flake thermal resistances, the various amounts of functional groups, and flake lateral dimension distribution in filtrated $Ti_3C_2T_x$ film, the disparity between simulated and experimental results remains unclear. More efforts to reveal the mechanisms behind hot carrier contribution are urgently needed.

2.2 Anisotropic thermal transport in MXenes

Similar to other 2D materials such as graphene, boron nitride, etc., MXenes flakes are expected to possess anisotropic thermal conductivity in both the cross-plane and in-plane direction due to the strong covalent bond in the basal plane and the weak interlayer interaction such as VDWs forces and hydrogen bond. Furthermore, the detailed anisotropic thermal conductivity of

Table 2 Selected experimental thermal conductivity of MXenes family at room temperature [63–66]

MXenes	Thermal conductivity κ ($W \cdot m^{-1} \cdot K^{-1}$)	Samples	Methods	Years	Ref.
$Ti_3C_2T_x$	2.84	Filtrated film	Steady-state T-type	2018	[65]
$Ti_3C_2T_x$	55.2 ± 1.7	Flake	Temperature-dependent Raman spectroscopy/polarized-laser power-dependent Raman spectroscopy	2018	[66]
$Ti_3C_2T_x$	2.45	Dip-coating film	Transient electro-thermal (TET)	2022	[63]
$Ti_3C_2T_x$	13.62 ± 0.23	Filtrated film	Transient electro-thermal (TET)	2022	[64]

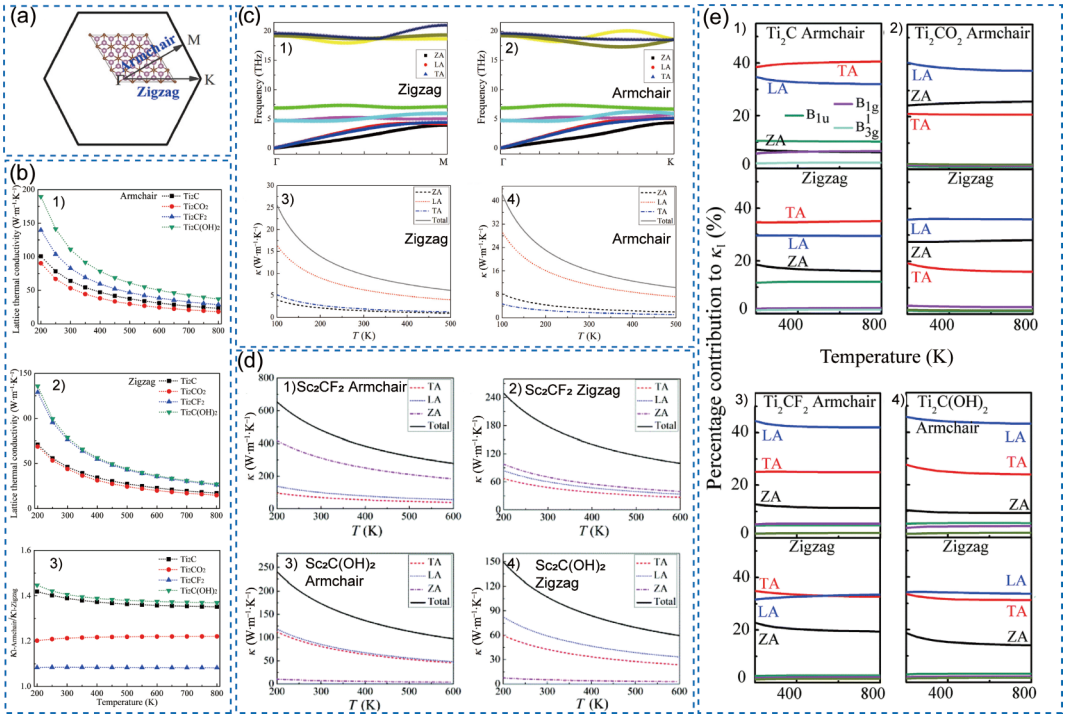

Figure 4 (a) Illustrate of armchair and zigzag direction of the hexagonal lattice. Reproduced with permission from Ref. [51], © American Chemical Society 2016. (b) The lattice thermal conductivities (1, 2) and thermal conductivity ratio (3) of Ti_2CT_2 along the armchair and zigzag directions. Reproduced with permission from Ref. [59], © Royal Society of Chemistry 2018. (c) The phonon dispersions (1, 2) and thermal conductivities (3, 4) of Mo_2C along the zigzag and armchair directions, respectively. Reproduced with permission from Ref. [51], © American Chemical Society 2016. (d) The lattice thermal conductivities of the Sc_2CF_2 along the (1) armchair and (2) zigzag directions, and the thermal conductivities of the $Sc_2C(OH)_2$ MXene along the (3) armchair and (4) zigzag directions. TA, LA, and ZA denote different phonon branches. Reproduced with permission from Ref. [52], © Royal Society of Chemistry 2016. (e) Percentage contribution of each phonon branch of Ti_2CT_2 MXenes to lattice thermal conductivity along armchair and zigzag directions. Reproduced with permission from Ref. [59], © Royal Society of Chemistry 2018.

MXenes in the in-plane direction has also been investigated. Originating from the different phonon branches dispersion and contribution in the armchair and zigzag direction of the hexagonal lattice (Fig. 4(a)), the anisotropic lateral thermal conductivity in MXenes has been predicted [51, 52, 59]. As shown in Fig. 4(c), the room-temperature lattice thermal conductivity of Mo_2C reaches 11.9 and 18.2 $W \cdot m^{-1} \cdot K^{-1}$, along the zigzag and the armchair direction, respectively [51]. Anisotropic thermal transport in Sc_2CT_2 (T = –OH, –F) has also been predicted [52]. Take the Sc_2CF_2 as an example, the theoretical thermal conductivity value is 178 and 472 $W \cdot m^{-1} \cdot K^{-1}$ along the zigzag and armchair direction, the contribution of deferent phonon branches are denoted in Fig. 4(d), further investigation reveals that surface functional groups can also affect the in-plane thermal transport anisotropy, and $Sc_2C(OH)_2$ is less anisotropic comparing with Sc_2CF_2 [52]. Simulation results of Ti_2CT_x (T = –O, –OH, –F) confirm the universal anisotropic thermal transport in MXene materials. The predicted thermal conductivities of Ti_2C, Ti_2CO_2, $Ti_2C(OH)_2$, Ti_2CF_2, and the percentage contributions of each phonon branch are shown in Figs. 4(b) and 4(e), respectively.

2.3 Effect of lateral dimension on MXenes thermal conductivity

Zha et al. simulated the thermal transport in oxygen-functionalized M_2CO_2 (whereas M = Ti, Zr, Hf) with the flake length ranging from 1 to 100 μm (Table 1 included the thermal conductivity of 5 μm MXenes flakes) [50]. Among them, the Hf_2CO_2 reached the highest theoretical value and exceeded the well-known 2D nanomaterials such as MoS_2 and phosphorene, etc. [50]. By varying the simulated MXenes flake length, the investigation results suggest that thermal conductivity value in both armchair and zigzag direction increased along with the elongation of flake length. To be more explicit, the lateral dimension dependence of Hf_2CO_2 thermal transport is shown in Figs. 5(a) and 5(b). As the flake length changed from 1 to 100 μm, the thermal conductivity of Hf_2CO_2 around room temperature increased from 62.12 to 131.2 $W \cdot m^{-1} \cdot K^{-1}$ in the armchair direction and 27.63 to 53.03 $W \cdot m^{-1} \cdot K^{-1}$ in zigzag direction, respectively [50]. As a result of finite flake length-induced boundary scattering, the length-dependent thermal conductivity trend in Hf_2CO_2 is ascribed to the limited minimum circular frequency of each phonon branch according to Klemens' theory [50]. Similarly, the flake-dependence thermal transport in Sc_2CF_2 has also been investigated. Based on the simulation results, the 5 μm Sc_2CF_2 reached a superior thermal conductivity value (427 $W \cdot m^{-1} \cdot K^{-1}$) which even surpasses many metallic conductors. As shown in Fig. 5(c), the room-temperature thermal conductivity of Sc_2CF_2 increased from 298 to 722 $W \cdot m^{-1} \cdot K^{-1}$ as the simulated flake length changed from 1 to 50 μm [52].

2.4 Effect of a surface functional group on MXenes thermal conductivity

Highly tunable thermal conductivity is of great importance for thermal management and thermoelectric applications. Modulating the thermal and electric properties of MXenes through terminal groups' doping effect has been reported as a practical approach [5, 59, 60, 69]. Terminal groups induced thermal conductivity discrepancy can range in one magnitude (Table 1). Systematically study for the terminal dependent on MXene electronic structure suggested that $Ti_3C_2T_x$ bandgap is in the range of 3.9–4.8 eV from both density functional theory (DFT) calculation and measured angle-resolved photoemission spectroscopy (ARPES) [70, 71]. Band dispersion varieties induced by terminal species further affect effective mass, valley degeneracy, etc. crucial parameters for high thermoelectric efficiency. Recently reported $Ti_3C_2T_x$/$(Bi, Sb)_2Te_3$ composite reached an average ZT value of 1.23 and attributed the simultaneous thermal conductivity decrease and electrical conductivity improvement to the oxygen-terminated

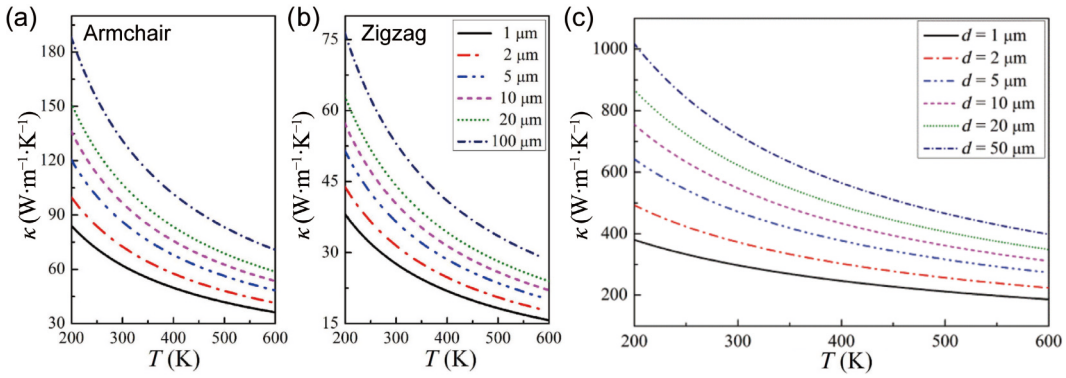

Figure 5 (a) The temperature-dependent Hf_2CO_2 thermal conductivity with varying flake lengths in the armchair direction. Reproduced with permission from Ref. [50], © Zha, X.-H. et al. 2016. (b) The temperature-dependent Hf_2CO_2 thermal conductivity with varying flake lengths in the zigzag direction. Reproduced with permission from Ref. [50], © Zha, X.-H. et al. 2016. (c) The temperature-dependent Sc_2CF_2 thermal conductivity with varying flake lengths in the armchair direction. Reproduced with permission from Ref. [52], © Royal Society of Chemistry 2016.

induced hole injection and suppressed phonon transport, respectively [70]. However, the fundamental mechanisms behind the termination-engineered MXenes remain unclear. Early in 2016, Kumar et al. studied the electronic and thermal behavior of Sc_2C modified with –O, –F, and –OH groups. Sc_2CO_2 reached the highest lattice thermal conductivity among them (~ 59 $W·m^{-1}·K^{-1}$) and $Sc_2(OH)_2$ exhibited the lowest lattice thermal conductivity (~ 10 $W·m^{-1}·K^{-1}$) because of the largest anharmonic phonon scattering (Fig. 6(a)) [45]. Guo et al. reported the systematically simulated result of Ti_2CT_2 (whereas T = –OH, –F, and O) with tunable thermal conductivity and concluded that both –OH and –F functionalized Ti_2C exhibited improved thermal transport properties, while –O functionalized Ti_2C surface functionalization enhanced the phonon group velocity and specific heat in MXenes lattice, the different effects on thermal conductivity can be attributed to the significantly shorter phonon relaxation time, and reduced electron thermal conductivity result from metal-semiconductor transition in the case of Ti_2CO_2 (Fig. 6(b) [59]. Gholivand et al. reported the effect of surface terminations on the lattice thermal conductivity of monolayer $Ti_3C_2T_x$ MXenes (whereas T = –O, and –F), and the prediction results suggest that the thermal conductivity of $Ti_3C_2F_2$ (108 $W·m^{-1}·K^{-1}$) exceeded its oxygen-terminated counterpart $Ti_3C_2O_2$ (11 $W·m^{-1}·K^{-1}$) for one order of magnitude (Fig. 6(c)) [61]. This is due to the stronger interaction in the $Ti_3C_2O_2$ lattice leads to shorter relaxation time and lower phonon group velocity, which aligned well with the research of Guo et al. [59].

In addition to the type of terminal groups, the effect of different termination configurations has also been investigated. Sarikurt et al. simulated the lattice thermal conductivity of –O surface-modified M_2CO_2 (whereas M = Ti, Zr, Hf, Sc) with different crystal configurations MD-II and MD-III (Fig. 6(e)) [60]. Among them, the theoretical thermal conductivity of MD-III Sc_2CO_2 reached the highest thermal conductivity ~ 57.01 $W·m^{-1}·K^{-1}$ (Fig. 6(d)) at room temperature, which is in good agreement with the previous study from Kumar et al. (~ 59 $W·m^{-1}·K^{-1}$) [45]. Furthermore, All three M_2CO_2 exhibited smaller thermal conductivity as the terminal group configuration changed from the symmetric MD-II lattice to the asymmetric MD-III lattice. This disparity is attributed to the enhanced scattering of the ZA mode phonons in the MD-III as a result of reduced crystal symmetry [60]. In sharp contrast with this work, recently, Lu et al. reported different prediction results on the relationship between crystal symmetry and thermal transport of Ta_2CS_2 (Fig. 6(f)) [46]. By breaking inversion symmetry in Ta_2CS_2 lattice, the anharmonic phonon scattering in asymmetric configuration is reduced by one

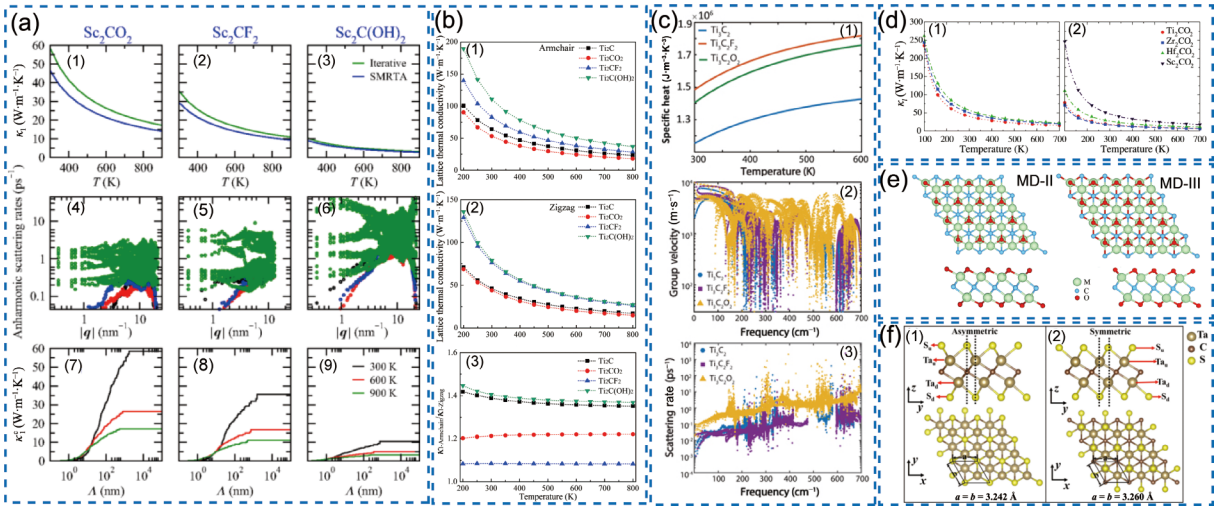

Figure 6 (a) Lattice thermal conductivities, room-temperature anharmonic scattering rates (black, red, blue, and green color denote the ZA, TA, LA, and optical phonon branches, respectively), and cumulative lattice thermal conductivities of Sc_2CT_2. Reproduced with permission from Ref. [45], © American Physical Society 2016. (b) The lattice thermal conductivities (1, 2) and thermal conductivity ratio (3) of Ti_2CT_2 along the armchair and zigzag directions. Reproduced with permission from Ref. [59], © Royal Society of Chemistry 2018. (c) Phonon volumetric specific heat, group velocity, and scattering rate of $Ti_3C_2T_x$ monolayer MXenes. Reproduced with permission from Ref. [61], © American Institute of Physics 2019. (d) Temperature-dependent thermal conductivities of M_2XT_2 MXene (whereas M = Ti, Zr, Hf, Sc) with crystal configurations MD-II and MD-III. Reproduced with permission from Ref. [60], © Royal Society of Chemistry 2018. (e) Schematic of crystal configurations MD-II and MD-III. Reproduced with permission from Ref. [60], © Royal Society of Chemistry 2018. (f) Schematic of asymmetric and symmetric crystal configuration of Ta_2CS_2. Reproduced with permission from Ref. [46], © American Physical Society 2022.

order of magnitude and results in a higher thermal conductivity, they stated that the more intense phonon scattering in symmetric configuration can be ascribed to the softened TO branch and the larger amplitude of atomic vibrations in symmetric Ta_2CS_2 [46].

Despite the inspirational prediction of thermal conductivity obtained from monolayered or single functional group modified MXenes, there is a significant gap between the experimental data and simulation values. An earlier reported thermal conductivity value of filtrated $Ti_3C_2T_x$ film has been measured as 2.84 $W \cdot m^{-1} \cdot K^{-1}$ around room temperature, which is a substantial deviation from expectations [69]. Considering the significant effects on thermal transport properties, further elucidation of the terminal groups occupancy ratio and strategies for the rational design of MXenes with controllable specific surface modifications are of great interest. Early in 2018, Persson et al. investigated the thermal behavior of $Ti_3C_2T_x$ and coordinated the surface groups at the atomic level by temperature-programmed X-ray photoelectron spectroscopy technique (TP-XPS) [72]. This study suggests that –F and –O group compete for the thermodynamically preferred site predicted by DFT, and the –F speice dominates at lower temperatures [72]. Hart et al. reported an effective in situ vacuum annealing and intercalation method for tailoring the termination of $Ti_3C_2T_x$. This fundamental work is not only of great importance for MXenes-based electronic applications but also brings opportunities into the thermal transport in MXenes [73].

2.5 Measured MXenes thermal conductivity and advanced techniques for MXenes thermal properties characterization

Despite the large number of advances in MXenes thermal transport simulation, experimental evidence is somewhat limited [63–66]. The reported experimental values of MXene thermal conductivity and techniques are summarized in Table 2.

Chen et al. first reported the experimental thermal conductivity of filtrated $Ti_3C_2T_x$ film with the steady-state T-type method [65]. The schematic of the T-type technique is shown in Fig. 7(a). The free-stand $Ti_3C_2T_x$ film was cut into strips, and the ends were attached to the platinum hotwire and copper electrode, respectively [65]. The thermal conductivity of sample (κ_s) can be written as Eq. (7) [65, 74]

$$\kappa_s = \frac{L_s L_h \kappa_h A_h (L_h^3 q_V - 12 L_h \kappa_h \Delta T_V)}{L_{h1} L_{h2} A_s [12 L_h \kappa_h \Delta T_V - q_V (L_{h1}^3 + L_{h2}^3)]} \tag{7}$$

whereas L_s is the sample length between the suspended bridge, $L_h = L_{h1} + L_{h2}$ is the hot wire length. A_s and A_h are the cross-section area of the sample and hot wire, respectively. κ_h is the thermal conductivity of the hot wire, $q_V = UI/L_h A_h$ is defined as the volumetric heating power of the hot wire, and ΔT_V represent the volumetric average temperature rise of the hot wire.

The experimental thermal conductivity of filtrated $Ti_3C_2T_x$ film reached 2.84 $W \cdot m^{-1} \cdot K^{-1}$ at room temperature, which shows a great gap from the simulation results. The simplified thermal resistance model was induced to analyze the difference, but the essential factor of this modest thermal conductivity value remains obscure [65]. Despite the lack of a precise interpretation between the effective and intrinsic thermal conductivity value in the $Ti_3C_2T_x$ sample, the T-type technique provides the capability to measure sample thermal conductivity over a wide range of temperatures (from 2.8 to 300 K) and the requirement of sample thickness can be as low as tens of microns, which is beyond the availability of many techniques [65].

Raman spectroscopy is a well-known powerful tool for studying material structure information and thermal transport behavior [75, 76]. Thanks to their noncontact setup, material-specific nature, and unique test scope in micro/nanoscale, Raman-based techniques possess irreplaceable merit compared with traditional thermometry methods in low dimensional materials thermal properties characterization [76–78]. Advanced Raman-based techniques such as time-domain differential Raman (TD-Raman) [79], frequency-resolved Raman (FR-Raman) [80, 81], energy transport state-resolved Raman (ET-Raman) [20, 82–86], and frequency-domain energy transport state-resolved Raman (FET-Raman) [87], etc., with unique advantages have further been developed and widely used. Liu et al. characterized the thermal transport in $Ti_3C_2T_x$ Flake using the temperature-dependent and power-dependent polarized-laser Raman spectra, the thermal conductivity result is 55.2 ± 1.7 $W \cdot m^{-1} \cdot K^{-1}$. It is worthwhile to mention that detailed sample dimension, surface termination type, and local topology information of the intrinsic thermal conductivity characterization remains unclarified. The polarized-laser Raman spectra experiment setup is shown in Fig. 7(b), The vibration frequency of Raman active optical phonons is sensitive to local temperature fluctuations. As the test laser power increases, the localized laser heating effect becomes more obvious and the Raman peaks of the E_g^1 vibration exhibit a frequency redshift. For $Ti_3C_2T_x$ with two-dimensional structures, the relationship between thermal conductivity (κ) and power-dependent Raman shift can be described in Eq. (8)

$$\kappa = \chi \left(\frac{1}{2\pi h}\right) \left(\frac{\partial}{\partial P}\right)^{-1} \tag{8}$$

whereas χ is the first temperature coefficient of the E_g^1 vibration mode in $Ti_3C_2T_x$, h is the thickness of $Ti_3C_2T_x$, and the Raman shift coefficient can be obtained from the linear fitting result of the Raman-shift vs. laser power relationship in Polarized-laser power-dependent Raman spectra.

Considering the metallic electrical conductivity of $Ti_3C_2T_x$, characterizing the thermal properties by transient electro-thermal (TET) technique is a reliable choice. The TET technique schematic is shown in Fig. 7(c). The sample was suspended between electrodes and attached with conductive silver paste, the step current was applied between two electrodes and generated Joule heat in the sample. The sample undergoes a transient temperature rise and eventually reaches a steady-state thermal equilibrium, eventually. Heat convection effect is ruled out by conducting measurements in a vacuum chamber and a one-dimension thermal conduction model was adopted for the test (as shown in Eq (9)).

$$\rho C_P \frac{\partial T}{\partial t} = \kappa \frac{\partial^2 T}{\partial x^2} + q_0 \tag{9}$$

whereas ρ is the density, C_P is the specific heat, κ is the thermal conductivity, and q_0 is the heating power per unit volume.

The voltage variation over the sample represents the temperature change, and can be used to probing the temperature evolution. The temperature evolution can be expressed by Eq. (10)

$$T(t) = T_0 + \frac{8 q_0 L^2}{\kappa \pi^4} \sum_{m=1}^{\infty} \frac{1 - \exp[-(2m-1)^2 \pi^2 \alpha t / L^2]}{(2m-1)^4} \tag{10}$$

whereas L is the length of sample, α is the thermal conductivity and can be obtain by fitting the temperature rise curve with time t.

The normalized temperature increasing $T^*(t)$ defined as $T^*(t) = [T(t) - T_0] / [T(t \to \infty) - T_0]$ can be obtained by Eq. (11)

$$T^* = \frac{8 q_0 L^2}{\pi^4} \sum_{m=1}^{\infty} \frac{1 - \exp[-(2m-1)^2 \pi^2 \alpha t / L^2]}{(2m-1)^4} \tag{11}$$

The thermal conductivity of the sample can be calculated by Eq. (12) when the sample achieves the final steady-state (T_∞).

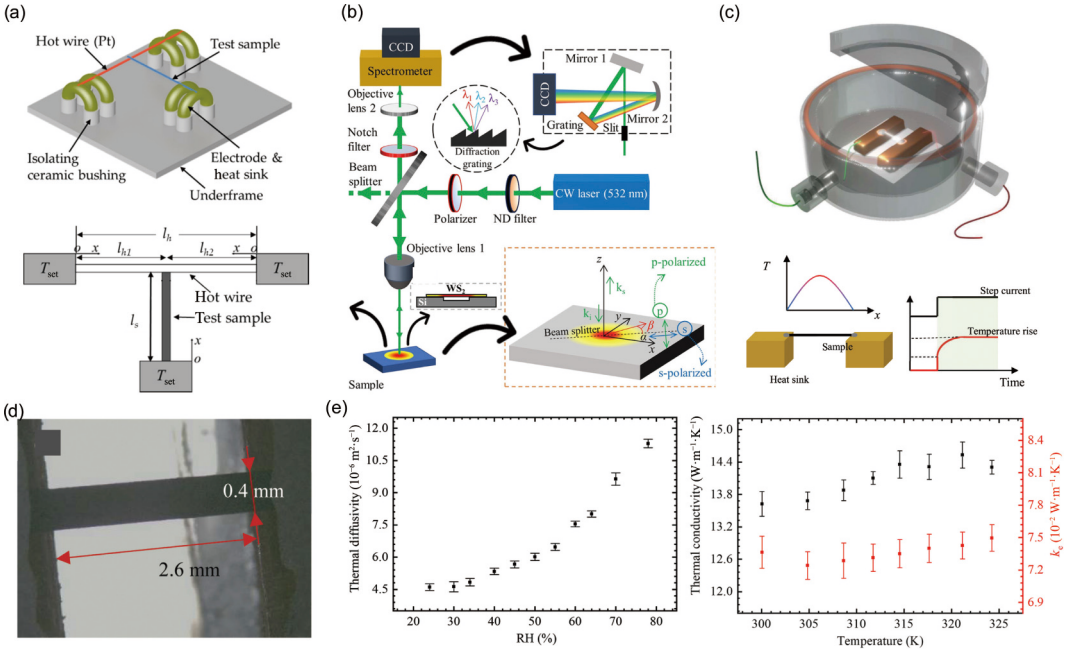

Figure 7 (a) Schematic (left) and physical mode (right) of the T-type method. Reproduced with permission from Ref. [65], © Chen, L. et al. 2018. (b) Schematic of polarized Raman system. Reproduced with permission from Ref. [77], © American Chemical Society 2019. (c) Schematic of experiment setup by TET technique (left), the physical model of the temperature rise and process of temperature rise of the sample (right). Reproduced with permission from Ref. [63], © IOP Publishing Ltd 2022. (d) The optical image of the $Ti_3C_2T_x$ sample in ref. 63 pasted between heat sinks. Reproduced with permission from Ref. [63], © IOP Publishing Ltd 2022. (e) Relative humidity-dependent thermal diffusivity (left) and temperature-dependent thermal conductivity/thermal diffusivity of $Ti_3C_2T_x$ sample. Reproduced with permission from Ref. [64], © Royal Society of Chemistry 2022.

$$\kappa = \frac{q_0 L^2}{12(T_\infty - T_0)} \tag{12}$$

Recently, Wu et al. reported the thermal conductivity of dip-coating $Ti_3C_2T_x$ film measured by the TET technique from 307 to 352 K, and the sample thermal conductivity increased from 2.45 to 2.81 $W \cdot m^{-1} \cdot K^{-1}$ [63]. The sample setup is shown in Fig. 7(d), and thermal conductivity-temperature dependence can be explained as the combined effect of increasing specific heat capacity and decreasing mean free path [63]. Yu et al. investigated the thermal transport response of filtrated $Ti_3C_2T_x$ film under different humidity environments using the TET technique [64]. The humidity dependence and temperature dependence of thermal properties are shown in Fig. 7(e). The room-temperature thermal conductivity of $Ti_3C_2T_x$ film is measured as 13.62 ± 0.23 $W \cdot m^{-1} \cdot K^{-1}$. As the environmental humidity increased, the thermal diffusivity and thermal conductivity of $Ti_3C_2T_x$ film decreased, this can be attributed to the low thermal conductivity of water (~ 0.598 $W \cdot m^{-1} \cdot K^{-1}$), the simulation result further confirmed this trend [64].

3 Advances in MXenes-based composite's thermal properties studies

Effective thermal dissipation in packaged microelectronics has become a crucial challenge to maintain good performance with the escalating trend of energy density in modern devices. Thermal management materials such as heat spreaders and thermal interface management materials (TIMs) play key roles in the increasing cooling demand of the modern electronic industry. TIMs with excellent thermal conductivity and flexibility can reduce the thermal resistance between heat-generating components and heat sink, providing a more efficient thermal transport pathway. The thermal resistance of TIMs can be expressed as a series of bulk thermal resistance of the TIMs and thermal contact resistances at the interface (Eq. (13)).

$$R_{TIMs} = \frac{BLT}{A\kappa_{TIMs}} + R_{c1} + R_{c2} \tag{13}$$

whereas κ_{TIMs} is the thermal conductivity of TIMs. BLT, A, R_{c1}, and R_{c2} are the bond line thickness, contact area, and contact resistances between the interfaces, respectively.

Thanks to their irreplaceable processability, flexibility, and cost-effectiveness, polymer-based TIMs have attracted growing interest and can efficiently reduce the thermal resistance between heat-generating components by decreasing the BLT, R_{c1}, and R_{c2}. However, common polymers' modest thermal transport capability severely limited their potential in thermal interface materials (TIMs) applications, reinforcements with outstanding thermal transport capability are expected to solve this drawback. As the experimental and theoretical research we discussed above has suggested, MXenes are appealing reinforcements of polymer-based thermal management materials for superior intrinsic thermal conductivity, good mechanical properties, chemical stability, and the presence of various functional groups.

At the other extreme of heat dissipation, superior electromagnetic interference (EMI) shielding materials with ultralow thermal conductivity are desired and expected to prevent the sensitive electronics from both external electromagnetic radiations and temperature fluctuations simultaneously. Recently reported MXene polymeric composites have shown great potential in EMI applications [88–90]. The MXene/aramid nanofibers/polyimides EMI porous aerogels with merely 0.045 $W \cdot m^{-1} \cdot K^{-1}$ thermal conductivity realized excellent Joule heating insulation performance [88]. MXene@Ag/polyvinyl alcohol films fabricated by the evaporative self-assembly method successfully constructed the heterostructure EMI materials with anisotropic thermal transport properties, reaching through-plane conductivity as low as 0.41 $W \cdot m^{-1} \cdot K^{-1}$ [89]. To better understand the potential of the MXene polymeric composites and provide more insight into thermal dissipation issues, we discussed the fundamentals behind MXene-enabled thermal transport composites, the critical parameters, advanced thermal management materials manufacturing techniques, synergetic effect in multi-filler systems are also highlighted. The represented advances in MXene composites are summarized in Table 3.

3.1 Understanding the thermal transport in MXenes-polymer composites

To accurately tailor thermal transport in heterogenous materials, it is of great importance to understand the interplay between polymeric matrix and fillers. Various empirical, analytical, and numerical models are developed to predict thermal transport capability in heterogeneous materials [114]. The rule of mixture (Eq. (14)) provided a simple picture for binary composites by assuming a linear combination of thermal conductivity from individual components.

$$\kappa_{\text{eff}} = V_{\text{f}}\kappa_{\text{f}} + V_{\text{m}}\kappa_{\text{m}} \quad (14)$$

whereas κ_{eff} is the effective thermal conductivity of composites, $V_{\text{f}}/V_{\text{m}}$ and $\kappa_{\text{f}}/\kappa_{\text{m}}$ are the volume fraction and thermal conductivity of filler/matrix, respectively. However, this simple model failed to take account into various factors in composites such as the filler orientation, filler shape, and size, interfacial thermal resistance, etc. More sophisticated models have been developed for different constituents. Percolation theory provides good predictions of effective thermal conductivity when the embedded nanostructures fraction reaches the critical threshold and forms a thermally conductive network [115]. For dilute composites, effective medium approximation (EMA) is extensively accepted for effective thermal conductivity prediction with fillers loading ratio below the percolation threshold, the fundamental model of EMA is the Maxwell–Garnett (M–G) model and can be expressed in Eq. (15) [116, 117]

$$\kappa_{\text{eff}} = \kappa_{\text{m}} \frac{2\kappa_{\text{m}} + \kappa_{\text{f}} + 2f(\kappa_{\text{f}} - \kappa_{\text{m}})}{2\kappa_{\text{m}} + \kappa_{\text{f}} - 2f(\kappa_{\text{f}} - \kappa_{\text{m}})} \quad (15)$$

whereas κ_{f}, κ_{m} are thermal conductivity of filler and matrix,

Table 3 Thermal transport performance of current reported MXenes-polymer composites

MXene	Matrix	Thermal conductivity κ ($W \cdot m^{-1} \cdot K^{-1}$)	Loading ratio	Note	Years	Ref.
$Ti_3C_2T_x$	Poly(vinylidene fluoride)	0.363	5 wt.%	Solution casting + hot pressing film	2017	[91]
$Ti_3C_2T_x$	Poly(vinyl alcohol)	47.6	—	Filtrated film	2018	[66]
Ti_3C_2/Ag	Epoxy	7.60 (in-plane) 0.61 (through-plane)	15 wt.%	Tertiary filler/bar coating film	2018	[92]
Ti_3C_2	Epoxy	0.587	1 wt.%	Solution casting film	2019	[93]
$Ti_3C_2T_x$	Nitrile butadiene rubber	1.01	19.6 vol.%	Latex compounding film	2020	[94]
$Ti_3C_2T_x$	Epoxy	3.14 (in-plane) 0.294 (through-plane)	30 wt.%	Cured disk	2020	[95]
Ti_3C_2/CF	Epoxy	9.68	30.2 wt.%	Freeze-drying 3D filler foam	2020	[37]
Ti_3C_2/Ag	Epoxy	2.65	15.1 vol.%	Tertiary filler/ice-templated 3D filler aerogels	2020	[96]
$Ti_3C_2T_x$	Poly (vinyl alcohol)	4.57	19.5 wt.%	Layer-by-layer casting	2020	[97]
$Ti_3C_2T_x$	Polyvinyl chloride	3.48	10 wt.%	Solution casting film	2020	[98]
$Ti_3C_2T_x$	(PDMS)	0.64 ± 0.013	2.5 vol.%	Vacuum-assisted impregnation	2020	[99]
$Ti_3C_2T_x$	Polyurethane	6.31 (in-plane) 0.42 (through-plane)	28.6 wt.%	Layer-by-layer casting	2021	[100]
$Ti_3C_2T_x$	Polyimide	5.12 ± 0.37 (in-plane) 0.28 ± 0.006 (through-plane)	40 wt.%	Freeze-drying/hot-pressing	2021	[38]
$Ti_3C_2T_x$	Epoxy	0.29	1 wt.%	Cured film	2021	[101]
Ti_3C_2-h-SiO_2	Styrene-butadiene rubber	0.401	6 wt.%	Electrostatic self-assembly	2021	[102]
MXenes/AgMPs/AgNPs	Epoxy	72.7	0.12 vol.% (MXenes) 50.12 vol.% (AgMP/AgNP = 1:3)	Tertiary filler	2021	[103]
$Ti_3C_2T_x$/SiO_2	Cellulose nanofibril	26.4	2 wt.%	Vacuum-assisted self-assembly 3Dskeleton/*in-situ* grown SiO_2	2021	[104]
$Ti_3C_2T_x$	Cellulose nanofibril	14.93 (in-plane)	60 wt.%	Vacuum-assisted self-assembly	2021	[105]
$Ti_3C_2T_x$/AgNW	Cellulose nanofibril	15.53 (in-plane) 0.32 (through-plane)	50 wt.%	Layer-by-layer casting	2021	[106]
$Ti_3C_2T_x$/AgNW	Epoxy	2.34	3.2 wt.%	Directional freeze-drying	2022	[107]
$Ti_3C_2T_x$/MWCNTs/Fe_3O_4	Polyethylene glycol	8.241	—	Layer-by-layer casting	2022	[108]
Ti_3C_2/Cu	Cellulose nanofibril	24.96 (in-plane) 2.46 (through-plane)	27.94 vol.% (Ti_3C_2) 23.74 vol.% (Cu)	High-speeding shear mixing/filtrated film	2022	[109]
$Ti_3C_2T_x$	Microcrystalline cellulose	9.668 (in-plane)	30 wt.%	Solution casting film	2022	[110]
$Ti_3C_2T_x$/BNNSs	Polymethyl methacrylate	4.13	20 wt.%	Electrostatic adsorption/hot pressing	2023	[111]
$Ti_3C_2T_x$/CNT	Polyethylene glycol	1.8	40 wt.%	Freeze-drying	2023	[112]
$Ti_3C_2T_x$	Mannitol	36.3 (in-plane) 1.06 (through-plane)	—	Vacuum-assisted filtration	2023	[113]

respectively, and f represents the filler volume fraction.

Despite the superior thermal conductivity of intrinsic MXenes materials (summarized in Tables 1 and 2), the effective thermal conductivities of MXene-polymeric composites exhibit inferior thermal conductivities (lower than 10 $W \cdot m^{-1} \cdot K^{-1}$), which are not even close to the reported theoretical and experiment value of MXenes fillers. The significant decrease in thermal conductivity not only results from the poor thermal conductivity of the polymeric host (~ 0.2 $W \cdot m^{-1} \cdot K^{-1}$) but can also be attributed to the universal interfacial thermal resistance (ITR) between fillers and matrix. ITR can be described as the disturbance of heat flow that occurs at the interface between the constituents of composites, which refers to the combination of thermal contact resistance (TCR) and thermal boundary resistance (TBR). TCR results from poor mechanical and chemical bonding between constituent phases, and TBR originates from the physical properties differences between filler-matrix interface even assuming the perfect contact between two solid phases at the atomic level [114]. The vibrational modes and electrical properties mismatch at the solid-solid boundary leading to heat carriers scattering, and the probability of transmission after scattering will depend on available energy states on both sides of the interface, further resulting in TBR [118, 119]. The interfacial thermal resistance strongly suppressed thermal transport in heterogeneous mediums and resulted in a considerable gap between fillers' intrinsic thermal properties and composite counterparts.

Modified EMA models further extended the effective thermal conductivity prediction terrace. Hasselman–Johnson (H–J) model considered the interface thermal conductivity (h_c) and particle size (a) effect. The H–J model was developed for spherical and is written in Eq. (16) [120]

$$\kappa_{\text{eff}} = \kappa_{\text{m}} \frac{\left[2\left(\frac{\kappa_{\text{f}}}{\kappa_{\text{m}}} - \frac{\kappa_{\text{f}}}{ah_{\text{c}}} - 1\right)V_{\text{f}} + \frac{\kappa_{\text{f}}}{\kappa_{\text{m}}} + \frac{2\kappa_{\text{f}}}{ah_{\text{c}}} + 2\right]}{\left[\left(1 - \frac{\kappa_{\text{f}}}{\kappa_{\text{m}}} - \frac{\kappa_{\text{f}}}{ah_{\text{c}}}\right)V_{\text{f}} + \frac{\kappa_{\text{f}}}{\kappa_{\text{m}}} + \frac{2\kappa_{\text{f}}}{ah_{\text{c}}} + 2\right]} \tag{16}$$

For 2D materials such as graphene, boron nitride, and MXene, the H–J model developed flat plate dispersions oriented perpendicular to heat flow and provided a more accurate prediction (Eq. (17)) [120]

$$\kappa_{\text{eff}} = \kappa_{\text{m}} \frac{\kappa_{\text{f}}}{\left[\left(1 - \frac{\kappa_{\text{f}}}{\kappa_{\text{m}}} - \frac{\kappa_{\text{f}}}{ah_{\text{c}}}\right)V_{\text{f}} + \frac{\kappa_{\text{f}}}{\kappa_{\text{m}}}\right]} \tag{17}$$

Bruggeman–Landauer (B–L) model and Nan model are also widely accepted for complex composite system prediction. By including the effect of filler size, loading ratio, orientation, and interface thermal resistance, the Nan model enables a more general EMA model. Considering the geometry parameter for laminated flat plates, the Nan model can be further simplified (Eqs. (18) and (19)) [121]

$$\kappa_{\text{eff},x} = \kappa_{\text{eff},y} = (1 - V_{\text{f}})\kappa_{\text{m}} + V_{\text{f}}\kappa_{\text{f}} \tag{18}$$

$$\kappa_{\text{eff},z} = \kappa_{\text{m}} \frac{\kappa_{\text{f}}}{(\kappa_{\text{m}} - V_{\text{f}}(\kappa_{\text{m}} - \kappa_{\text{f}} - \alpha\kappa_{\text{m}})} \tag{19}$$

whereas the dimensionless parameter, κ is defined as the ratio of Kapitza radius in x, y-plane and z-axis [121]. The predicted z-axis effective thermal conductivity in Nan model shows consisted result the with H–J model.

Fabricating high thermal conductivity MXene composites is long desired. To sum up, the poor thermal transport capability of composite materials mainly originates from the weak filler-matrix interaction induced interface thermal resistance, and ineffective transport in intermittent medium. Considering the diversity of MXenes surface terminal types and the high aspect ratio of their two-dimensional materials feature, we summarized state-of-art research and discussed (1) the effective strategies for suppressing interface thermal resistance and manipulating the MXene-matrix interaction at the molecular level; (2) advanced manufacturing techniques for constructing effective thermal transport pathway. (3) The synergetic effect in multi-filler system was also highlighted.

3.2 Manipulating MXene-matrix interaction

Weak interaction between reinforced filler and polymer host is the main source of thermal resistance in heterogeneous composites. MXenes possess high thermal conductivity and adjustable surface functional groups (–OH, –F, –O), which provide abundant reactive sites for required modification and engineering interfacial interaction in polymer/MXenes thermal conductive composites. Liu et al. reported $Ti_3C_2T_x$/epoxy composites with improved thermal conductivity, the methyl tetrahydrophthalic anhydride (MTHPA) is chosen as a curing agent and reacts with the hydroxyl groups on the surface of $Ti_3C_2T_x$ to form a chemical bonding between the reinforcement and the matrix, further facilitate efficient thermal transport in composites, the diagrammatic sketch of reaction and resulted thermal conductivity enhancement are shown in Fig. 8(a) [101]. $Ti_3C_2T_x$/poly (vinyl alcohol) (PVA) composites with outstanding thermal stability and thermal conductivity ~ 47.6 $W \cdot m^{-1} \cdot K^{-1}$ have been reported, the enhancement can be attributed to the strong Ti–O bonds formed between the MXene and PVA host. The filler-matrix interaction is further confirmed by the X-ray photoelectron spectroscopy results and can be seen in Fig. 8(b) [66]. Aakyiir et al. developed both electrically and thermally conductive $Ti_3C_2T_x$/nitrile butadiene rubber (NBR) composites. The $Ti_3C_2T_x$ MXene nanosheets are modified by allylamine and form covalent bonding with the elastomer matrix. The schematic of composite synthesis is shown in Fig. 8(c) [94]. Mazhar et al. synthesized $Ti_3C_2T_x$/polyvinyl chloride (PVC) film with thermal conductivity reaching 3.48 $W \cdot m^{-1} \cdot K^{-1}$ at loading ratio of percolation threshold (10 wt.%). The intrinsic high electrical conductance of MXene results in charge aggregation at filler-matrix interfaces. The interfacial polarization provided stronger interaction, better dispersion, and compatibility between $Ti_3C_2T_x$ and PVC, further facilitating the construction of effective heat paths in composites Fig. 8(d)) [98]. Kong et al. reported $Ti_3C_2T_x$/mannitol film fabricated by vacuum-assisted filtration, the hydroxyl group in mannitol spontaneously binding onto titanium ions in MXene and thus realizing in-situ polymerization (Fig. 8(e)). The resulting composites reached superior in-plane thermal conductivity ~ 36.3 $W \cdot m^{-1} \cdot K^{-1}$ [113]. $Ti_3C_2T_x$/copper particles/cellulose nanofibers (CNF) film with superior in-plan thermal conductivities reached 24.96 $W \cdot m^{-1} \cdot K^{-1}$, which increased by 2819.2% compared with the polymeric matrix. The significant enhancement is credited to the esterification of the carboxyl group in the MXene surface and the hydroxyl groups in cellulose nanofibers. Chemical bonds between fillers and matrix facilitate the forming of the composite skeleton and thermal transport pathway [109].

3.3 Constructing MXenes thermal conductive network

Well-arranged filler networks can effectively suppress the thermal resistance arising from filler-matrix interface, and continuous heat conduction channels for the transmission of electrons and phonons to enhance composites' thermal transport capabilities [122]. Adjusting filler orientation and constructing thermally conductive 3D network structure, further facile directional heat dissipation is highly desired in thermal management applications. MXenes with higher aspect ratio and anisotropic thermal properties are expected to enhance composites thermal properties

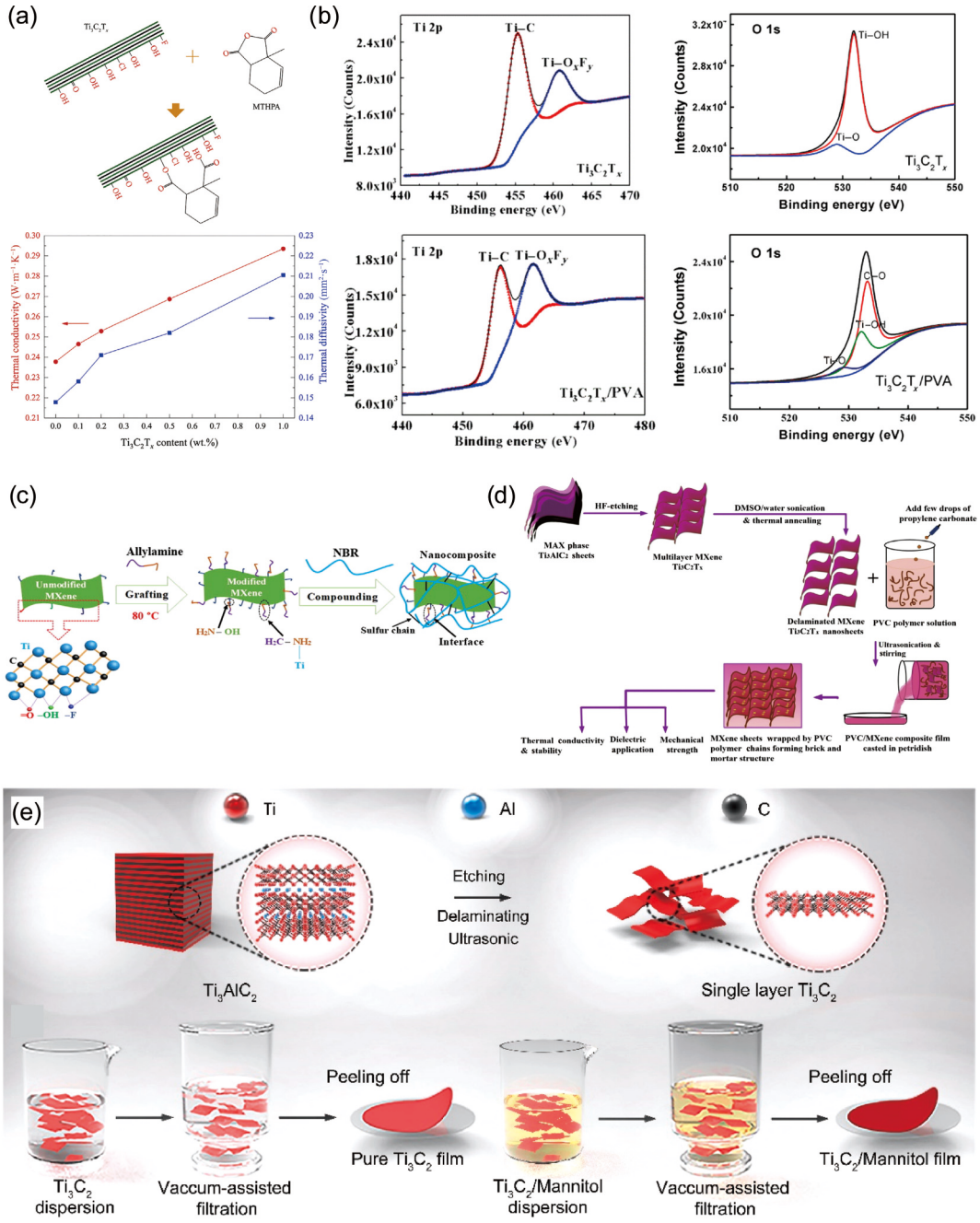

Figure 8 (a) Schematic of the bonding formed through chemical reactions between MTHPA and $Ti_3C_2T_x$. Composites thermal conductivities and thermal diffusivities under different $Ti_3C_2T_x$ loading content. Reproduced with permission from Ref. [101], © Elsevier Ltd. 2020. (b) High-resolution Ti 2p and O 1s XPS images of $Ti_3C_2T_x$ MXene and $Ti_3C_2T_x$/PVA composite. Reproduced with permission from Ref. [66], © Liu, R. et al. 2018. (c) Schematic of $Ti_3C_2T_x$ modification and $Ti_3C_2T_x$/nitrile butadiene rubber (NBR) composite formation. Reproduced with permission from Ref. [94], © Elsevier B.V. 2020. (d) Schematic of $Ti_3C_2T_x$ synthesis and $Ti_3C_2T_x$/PVC fabrication. Reproduced with permission from Ref. [98], © Elsevier Ltd. 2020. (e) Schematic of $Ti_3C_2T_x$ synthesis and $Ti_3C_2T_x$/mannitol composite fabrication via vacuum-assisted filtration. Reproduced with permission from Ref. [113], © Elsevier Ltd. 2023.

through rational design and distribution of aligned structure, specific techniques including hot-pressing [38, 92], Freeze-drying [38, 96, 99, 107], multi-layered casting [97, 100, 106, 108], electrostatic self-assembly [102, 111], vacuum-assisted filtration [99, 102, 105, 113], etc., have been applied for MXenes-polymeric composites development.

Ti_3C_2/epoxy composites have been reported with 1470% enhanced thermal conductivity at 30 wt.% loading ratio [95]. The enlarged filler aspect ratio is also attributed to the thermal properties anisotropy of composites, the in-plane/through-plane thermal conductivity is 3.14 and 0.294 $W·m^{-1}·K^{-1}$, respectively [95]. Yan et al. developed Ti_3C_2/silver nanowire epoxy composites with in-plane thermal conductivity reaching 7.6 $W·m^{-1}·K^{-1}$. Multi-layer Ti_3C_2 flakes and silver nanowires are bridged by the thermocompression technique, thanks to the geometry feature of quasi-2D Ti_3C_2 flakes and 1D silver nanowires, the anisotropy ratio of thermal conductivity in in-plane and cross-plane direction reached 12.45 $W·m^{-1}·K^{-1}$ [92]. $Ti_3C_2T_x$/silver nanoparticles skeleton were prepared by combining the ice-templating and freeze-drying methods. The ordered 3D interconnection of fillers endowed efficient thermal transport, resulting thermal conductivity of binary components aerogel/epoxy composites is 2.65 $W·m^{-1}·K^{-1}$, which is 1225 % higher than the pure epoxy matrix [96]. Layer-by-layer casting is feasible for film fabrication, alternating structure $Ti_3C_2T_x$/PVA films developed by this technique exhibited 23 times enhancement in in-plane thermal conductivity and outstanding flame-retardance [97]. Multilayered $Ti_3C_2T_x$/thermoplastic polyurethane (TPU) films achieved 6.31/0.42 $W·m^{-1}·K^{-1}$ in-plane

and through-plane thermal conductivity, respectively [100]. Asymmetric sandwich structural $Ti_3C_2T_x$/silver nanowires/cellulose films assembled by layer-by-layer method with superior in-plane thermal conductivity 15.53 $W·m^{-1}·K^{-1}$ have also been reported [106]. $Ti_3C_2T_x$-hybrid-SiO_2 fillers assembled by electrostatic force are reported by Ma et al. Yielded $Ti_3C_2T_x$-hybrid-SiO_2/styrene-butadiene rubber (SBR) composites achieved improvement in both electrical, mechanical, and thermal properties (0.401 $W·m^{-1}·K^{-1}$) [102]. Solution-casting $Ti_3C_2T_x$/microcrystalline cellulose film reached in-plane thermal conductivity ~ 9.668 $W·m^{-1}·K^{-1}$ by constructing the overlapping $Ti_3C_2T_x$ nanosheets thermal conduction network uniformly [110]. $Ti_3C_2T_x$/mannitol composite films fabricated by vacuum-assisted filtration exhibit a highly aligned tight structure, the in-plane thermal conductivity reached 36.3 $W·m^{-1}·K^{-1}$, which is 32.3 times higher than the through-plane counterpart [113].

3.4 Advances in multi-filler thermal management materials

Rational design and construction of heat pathways in multi-component systems can maximize the synergistic effect and improve composites' thermal transport capability. The synergetic effect takes advantage of fillers with different sizes and dimensions to form effective thermal conductive paths at relatively low total filler loading [92, 96, 102–104, 106–108, 111, 123]. $Ti_3C_2T_x$/silver particles aerogels were developed as thermal transferring skeletons and integrated into the epoxy matrix (Fig. 9(a)), Monte Carlo simulation suggests the effective reduced thermal interface resistance (4.5×10^{-7} $m^2·W^{-1}·K^{-1}$) compared with pure $Ti_3C_2T_x$/epoxy interface (5.2×10^{-7} $m^2·W^{-1}·K^{-1}$) [96]. $Ti_3C_2T_x$-hybrid-SiO_2 binary thermal fillers have also been reported, the presence of SiO_2 improved filler dispersion in the SBR matrix, and further immobilized the rubber chains during the curing process. The hybrid filler reinforced both the thermal and mechanical properties of composites [102]. 3D cross-linking thermal conductive skeleton constructed by *in-situ* grown SiO_2 nanoparticles and $Ti_3C_2T_x$ sheets have realized conspicuous enhancement of thermal conductivity in carboxymethylated CNF composites (Fig. 9(b) [104]. $Ti_3C_2T_x$ flake bridged by 2 wt.% SiO_2 nanoparticles achieved high in-plane thermal conductivity ~ 26.4 $W·m^{-1}·K^{-1}$. The strong hydrogen bonding interactions between SiO_2 nanoparticles and $Ti_3C_2T_x$ significantly decreased the filler agglomeration [104]. Tertiary filler system ($Ti_3C_2T_x$/silver microparticle AgMPs/silver nanoparticles AgNPs) incorporated in the epoxy matrix have realized ultrahigh thermal conductivity (72.7 $W·m^{-1}·K^{-1}$), which have suppressed many metal thermal conductors [103]. With merely 0.12 vol.% amount of $Ti_3C_2T_x$ added, the epoxy composites achieved 24.7% enhancement. Thanks to the various shapes and sizes of the tertiary filler system, the remarkable synergetic effect has been proved, and microstructural characteristics are shown in Fig. 9(d) [103]. $Ti_3C_2T_x$ /silver nanowires (AgNWs)/epoxy composites have been reported with thermal conductivity of 2.34 $W·m^{-1}·K^{-1}$ with only 8.2 wt.% loading ratio. Biocompatible sodium alginate (SA) with abundant oxygen-containing functional groups (–OH, –COOH, and =O) was induced to form strong hydrogen bonds between 1D silver nanowires and 2D $Ti_3C_2T_x$ which play a vital role in constructing the 3D thermal conductive network (Fig. 9(c)) [107]. The unique architecture of $Ti_3C_2T_x$/multi-walled carbon nanotubes (MWCNTs)/Fe_3O_4 nanoparticles has been reported, maximum thermal conductivity of 8.241 $W·m^{-1}·K^{-1}$ has been obtained [108]. Ti_3C_2/copper particles/cellulose nanofiber composites were prepared by shear mixing and vacuum-assisted filtration method. Deriving benefit from the synergistic effect of two types of fillers and the chemical bonding between MXene sheets and cellulose nanofibers matrix, the resulting composites film reached extraordinary in-plane thermal conductivity around 24.96 $W·m^{-1}·K^{-1}$. The diagram of the effective thermal conduction channel in composites is shown in Fig. 9(e) [109]. Boron nitride nanosheet (BNNSs) and $Ti_3C_2T_x$ hybrid filler self-assembling on PMMA sphere by electrostatic adsorption and hydrogen bond results in the core-shell structure in nanocomposites and exhibits effective thermal conductivity ~ 4.13 $W·m^{-1}·K^{-1}$. The thermal transport enhancement in composites is credited for not only the effective construction of 3D thermal pathways but also the BNNSs/PMMA hydrogen bonding and excellent BNNSs/$Ti_3C_2T_x$ phonon spectrum matching. The simulated phonon density of the state of BNNSs and $Ti_3C_2T_x$ based on the first-principles calculation is shown in Fig. 9(f). A large overlapping phonon spectrum area further confirmed the conclusion. Thanks to the stronger filler-matrix interaction and phonon spectrum similarity between different fillers, the interfacial phonon scattering can be effectively suppressed. The superior thermal conductivity enhancements and heat dissipation performances in MXene composites have demonstrated their feasibility in thermal

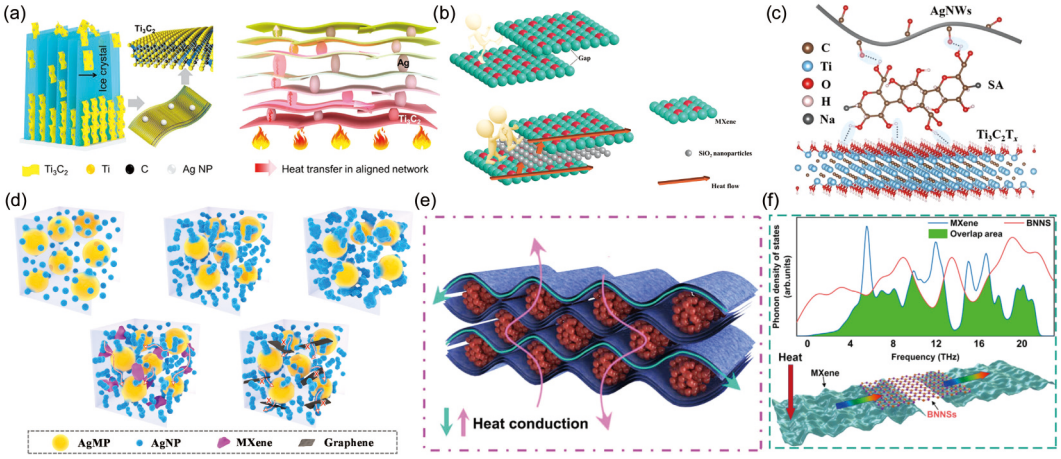

Figure 9 (a) Illustrate of ice-template technique for aligning the MXene/Ag nanofillers (left). Effective heat transfer in a welded MXene/Ag aerogel skeleton both in-plane and through-plane directions (right). Reproduced with permission from Ref. [96], © American Chemical Society 2020. (b) Schematic of thermal conductive mechanism in $Ti_3C_2T_x$-hybrid-SiO_2/carboxymethylated CNF composites. Reproduced with permission from Ref. [104], © Elsevier B.V. 2021. (c) Schematic of the interaction between $Ti_3C_2T_x$, sodium alginate (SA), and silver nanowires. Reproduced with permission from Ref. [107], © Elsevier B.V. 2021. (d) Schematic figure of microstructural characteristics of Ag/Epoxy composites. (with an increment of AgNP loading content, $Ti_3C_2T_x$/AgMP/AgNP, and graphene/AgMP/AgNP composites. Reproduced with permission from Ref. [103], © Elsevier B.V. 2021. (e) Schematic of thermal conduction in Ti_3C_2/copper particles/cellulose nanofiber composites. Reproduced with permission from Ref. [109], © Qin, Y. et al. 2022. (f) The phonon density of states vs frequency results of BNNSs/$Ti_3C_2T_x$ and schematic diagram of the thermal conduction model of BNNSs-MXene. Reproduced with permission from Ref. [111], © Elsevier Ltd. 2022.

management applications.

4 Conclusions and outlook

In summary, this review focused on the recent advances in thermal transport in MXenes and MXene-polymeric composites. The explosive growth of heat generation in modern devices has generated significant enthusiasm for research into thermal management materials. MXenes with rich structural, compositional diversities and unique combination of properties offer a fertile ground for tunable thermal conductive materials investigation. Most importantly, both theoretical prediction and experimental results have proved the superior intrinsic thermal transport capability in the first discovered MXene ($Ti_3C_2T_x$) and make MXenes a potential thermal management material for the next generation of heat dissipation technologies. To date, over 150 MAX precursors and 40 MXenes have been successfully synthesized, and the MXene family is continuously growing. However, most thermal property studies of MXene were focused on $Ti_3C_2T_x$, to our best knowledge, the experimental thermal conductivities of other MXenes have not been reported, and the fundamental understanding of thermal transport mechanisms in MXenes remains unclear. The complexity of MXenes thermal transport stems from the diversity of their constituent elements and the variety of surface termination species. To provide more clues for investigations of the large, underexplored family of MXenes, it is of great importance to study thermal transport in MXenes from both simulation and experiment aspects. We summarized the advanced thermal research in MXenes. Detailed aspects including heat carrier contribution, surface termination species, size-dependence thermal properties, and anisotropy in MXenes have been reviewed and discussed. Thermal property characterization techniques for MXene in different scopes were also discussed.

Exploring the fundamentals behind the micro-scale thermal transport mechanism would provide more insights for macro-scale heat dissipation applications. MXene-enabled thermally conductive polymeric composites have attracted significant research interest. Thanks to the combination of outstanding thermal conductivity, superior adhesion, flexibility, and highly adjustable filler-matrix interactions, MXene-polymer composites are expected to realize the rational design for next-generation thermal management materials. However, current MXene composites' thermal conductivity shows a considerable gap between the pure MXene counterpart. The heat dissipation capabilities are severely limited by the poor thermal transport in the polymeric matrix and the universal existing filler-matrix interfacial thermal resistance in MXene composites. In this review, effective modeling of heterogeneous materials was discussed to provide more insight for next-generation thermal management materials development. The essential factors for constructing MXenes thermal transport pathway in a polymeric matrix including the filler-polymer interaction, filler alignment, and synergetic effect in the multi-fillers system were also summarized.

Acknowledgments

This work is supported by the Office of Naval Research under Award Number N000142312569

References

[1] Naguib, M.; Kurtoglu, M.; Presser, V.; Lu, J.; Niu, J. J.; Heon, M.; Hultman, L.; Gogotsi, Y.; Barsoum, M. W. Two-dimensional nanocrystals produced by exfoliation of Ti_3AlC_2. *Adv. Mater.* **2011**, *23*, 4248–4253.

[2] Naguib, M.; Mochalin, V. N.; Barsoum, M. W.; Gogotsi, Y. 25th anniversary article: MXenes: A new family of two-dimensional materials. *Adv. Mater.* **2014**, *26*, 992–1005.

[3] Aghamohammadi, H.; Amousa, N.; Eslami-Farsani, R. Recent advances in developing the MXene/polymer nanocomposites with multiple properties: A review study. *Synth. Met.* **2021**, *273*, 116695.

[4] Khazaei, M.; Ranjbar, A.; Arai, M.; Sasaki, T.; Yunoki, S. Electronic properties and applications of MXenes: A theoretical review. *J. Mater. Chem. C* **2017**, *5*, 2488–2503.

[5] Khazaei, M.; Arai, M.; Sasaki, T.; Estili, M.; Sakka, Y. Two-dimensional molybdenum carbides: Potential thermoelectric materials of the MXene family. *Phys. Chem. Chem. Phys.* **2014**, *16*, 7841–7849.

[6] Jamil, F.; Ali, H. M.; Janjua, M. M. MXene based advanced materials for thermal energy storage: A recent review. *J. Energy Storage* **2021**, *35*, 102322.

[7] Wang, J. F.; Shen, M. M.; Liu, Z. X.; Wang, W. J. MXene materials for advanced thermal management and thermal energy utilization. *Nano Energy* **2022**, *97*, 107177.

[8] Moore, G. E. Progress in digital integrated electronics [Technical literaiture, Copyright 1975 IEEE. Reprinted, with permission. Technical Digest. International Electron Devices Meeting, IEEE, 1975, pp. 11-13.]. *IEEE Solid State Circ. Soc. Newsl.* **2006**, *11*, 36–37.

[9] Schelling, P. K.; Shi, L.; Goodson, K. E. Managing heat for electronics. *Mater. Today* **2005**, *8*, 30–35.

[10] Moore, A. L.; Shi, L. Emerging challenges and materials for thermal management of electronics. *Mater. Today* **2014**, *17*, 163–174.

[11] Cui, Y.; Li, M.; Hu, Y. J. Emerging interface materials for electronics thermal management: Experiments, modeling, and new opportunities. *J. Mater. Chem. C* **2020**, *8*, 10568–10586.

[12] El Sachat, A.; Alzina, F.; Sotomayor Torres, C. M.; Chavez-Angel, E. Heat transport control and thermal characterization of low-dimensional materials: A review. *Nanomaterials* **2021**, *11*, 175.

[13] Pop, E.; Varshney, V.; Roy, A. K. Thermal properties of graphene: Fundamentals and applications. *MRS Bull.* **2012**, *37*, 1273–1281.

[14] Chen, S. S.; Moore, A. L.; Cai, W. W.; Suk, J. W.; An, J.; Mishra, C.; Amos, C.; Magnuson, C. W.; Kang, J.; Shi, L. et al. Raman measurements of thermal transport in suspended monolayer graphene of variable sizes in vacuum and gaseous environments. *ACS Nano* **2011**, *5*, 321–328.

[15] Balandin, A. A.; Nika, D. L. Phononics in low-dimensional materials. *Mater. Today* **2012**, *15*, 266–275.

[16] Lindsay, L.; Broido, D. A. Enhanced thermal conductivity and isotope effect in single-layer hexagonal boron nitride. *Phys. Rev. B* **2011**, *84*, 155421.

[17] Sahoo, S.; Gaur, A. P. S.; Ahmadi, M.; Guinel, M. J. F.; Katiyar, R. S. Temperature-dependent Raman studies and thermal conductivity of few-layer MoS_2. *J. Phys. Chem. C* **2013**, *117*, 9042–9047.

[18] Liu, J.; Choi, G. M.; Cahill, D. G. Measurement of the anisotropic thermal conductivity of molybdenum disulfide by the time-resolved magneto-optic Kerr effect. *J. Appl. Phys.* **2014**, *116*, 233107.

[19] Yan, R. S.; Simpson, J. R.; Bertolazzi, S.; Brivio, J.; Watson, M.; Wu, X. F.; Kis, A.; Luo, T. F.; Hight Walker, A. R.; Xing, H. G. Thermal conductivity of monolayer molybdenum disulfide obtained from temperature-dependent Raman spectroscopy. *ACS Nano* **2014**, *8*, 986–993.

[20] Wang, R. D.; Wang, T. Y.; Zobeiri, H.; Yuan, P. Y.; Deng, C.; Yue, Y. A.; Xu, S.; Wang, X. W. Measurement of the thermal conductivities of suspended MoS_2 and $MoSe_2$ by nanosecond ET-Raman without temperature calibration and laser absorption evaluation. *Nanoscale* **2018**, *10*, 23087–23102.

[21] Yuan, P. Y.; Wang, R. D.; Wang, T. Y.; Wang, X. W.; Xie, Y. S. Nonmonotonic thickness-dependence of in-plane thermal conductivity of few-layered MoS_2: 2.4 to 37.8 nm. *Phys. Chem. Chem. Phys.* **2018**, *20*, 25752–25761.

[22] Sun, Z. M. Progress in research and development on MAX phases: A family of layered ternary compounds. *Int. Mater. Rev.* **2011**, *56*, 143–166.

[23] Gogotsi, Y.; Anasori, B. The rise of MXenes. *ACS Nano* **2019**, *13*, 8491–8494.

[24] Mathis, T. S.; Maleski, K.; Goad, A.; Sarycheva, A.; Anayee, M.; Foucher, A. C.; Hantanasirisakul, K.; Shuck, C. E.; Stach, E. A.;

Gogotsi, Y. Modified MAX phase synthesis for environmentally stable and highly conductive Ti_3C_2 MXene. *ACS Nano* **2021**, *15*, 6420–6429.

[25] VahidMohammadi, A.; Rosen, J.; Gogotsi, Y. The world of two-dimensional carbides and nitrides (MXenes). *Science* **2021**, *372*, eabf1581.

[26] Shahzad, F.; Alhabeb, M.; Hatter, C. B.; Anasori, B.; Man Hong, S.; Koo, C. M.; Gogotsi, Y. Electromagnetic interference shielding with 2D transition metal carbides (MXenes). *Science* **2016**, *353*, 1137–1140.

[27] Chen, N. J.; Yang, W. Q.; Zhang, C. F. Perspectives on preparation of two-dimensional MXenes. *Sci. Technol. Adv. Mater.* **2021**, *22*, 917–930.

[28] Alhabeb, M.; Maleski, K.; Anasori, B.; Lelyukh, P.; Clark, L.; Sin, S.; Gogotsi, Y. Guidelines for synthesis and processing of two-dimensional titanium carbide ($Ti_3C_2T_x$ MXene). *Chem. Mater.* **2017**, *29*, 7633–7644.

[29] Sang, X. H.; Xie, Y.; Lin, M. W.; Alhabeb, M.; Van Aken, K. L.; Gogotsi, Y.; Kent, P. R. C.; Xiao, K.; Unocic, R. R. Atomic defects in monolayer titanium carbide ($Ti_3C_2T_x$) MXene. *ACS Nano* **2016**, *10*, 9193–9200.

[30] Zamhuri, A.; Lim, G. P.; Ma, N. L.; Tee, K. S.; Soon, C. F. MXene in the lens of biomedical engineering: Synthesis, applications and future outlook. *Biomed. Eng. OnLine* **2021**, *20*, 33.

[31] Xu, C.; Wang, L. B.; Liu, Z. B.; Chen, L.; Guo, J. K.; Kang, N.; Ma, X. L.; Cheng, H. M.; Ren, W. C. Large-area high-quality 2D ultrathin Mo_2C superconducting crystals. *Nat. Mater.* **2015**, *14*, 1135–1141.

[32] Zhang, Z.; Zhang, F.; Wang, H. C.; Ho Chan, C.; Lu, W.; Dai, J. Y. Substrate orientation-induced epitaxial growth of face centered cubic Mo_2C superconductive thin film. *J. Mater. Chem. C* **2017**, *5*, 10822–10827.

[33] Xue, Q.; Zhang, H. J.; Zhu, M. S.; Pei, Z. X.; Li, H. F.; Wang, Z. F.; Huang, Y.; Huang, Y.; Deng, Q. H.; Zhou, J. et al. Photoluminescent Ti_3C_2 MXene quantum dots for multicolor cellular imaging. *Adv. Mater.* **2017**, *29*, 1604847.

[34] Zhao, S. J.; Kang, W.; Xue, J. M. MXene nanoribbons. *J. Mater. Chem. C* **2015**, *3*, 879–888.

[35] Lian, P. C.; Dong, Y. F.; Wu, Z. S.; Zheng, S. H.; Wang, X. H.; Wang, S.; Sun, C. L.; Qin, J. Q.; Shi, X. Y.; Bao, X. H. Alkalized Ti_3C_2 MXene nanoribbons with expanded interlayer spacing for high-capacity sodium and potassium ion batteries. *Nano Energy* **2017**, *40*, 1–8.

[36] Zhao, M. Q.; Xie, X. Q.; Ren, C. E.; Makaryan, T.; Anasori, B.; Wang, G. X.; Gogotsi, Y. Hollow MXene spheres and 3D macroporous MXene frameworks for Na-ion storage. *Adv. Mater.* **2017**, *29*, 1702410.

[37] Guo, L. C.; Zhang, Z. Y.; Li, M. H.; Kang, R. Y.; Chen, Y. P.; Song, G. C.; Han, S. T.; Lin, C. T.; Jiang, N.; Yu, J. H. Extremely high thermal conductivity of carbon fiber/epoxy with synergistic effect of MXenes by freeze-drying. *Compos. Commun.* **2020**, *19*, 134–141.

[38] Zhu, Y.; Zhao, X. B.; Peng, Q. Y.; Zheng, H. W.; Xue, F. H.; Li, P. Y.; Xu, Z. H.; He, X. D. Flame-retardant MXene/polyimide film with outstanding thermal and mechanical properties based on the secondary orientation strategy. *Nanoscale Adv.* **2021**, *3*, 5683–5693.

[39] Chen, G. *Nanoscale Energy Transport and Conversion: A Parallel Treatment of Electrons, Molecules, Phonons, and Photons*; Oxford University Press: Oxford, 2005.

[40] Lepri, S.; Livi, R.; Politi, A. Thermal conduction in classical low-dimensional lattices. *Phys. Rep.* **2003**, *377*, 1–80.

[41] Morelli, D. T.; Slack, G. A. High lattice thermal conductivity solids. In *High Thermal Conductivity Materials*. Shindé, S. L.; Goela, J. S., Eds.; Springer: New York, 2006; pp 37–68.

[42] Ziman, J. M. *Electrons and Phonons: The Theory of Transport Phenomena in Solids*; Clarendon Press: Oxford, 2001.

[43] Chen, G. Particularities of heat conduction in nanostructures. *J. Nanopart. Res.* **2000**, *2*, 199–204.

[44] Chen, G. Size and interface effects on thermal conductivity of superlattices and periodic thin-film structures. *J. Heat Transfer* **1997**, *119*, 220–229.

[45] Kumar, S.; Schwingenschlögl, U. Thermoelectric performance of functionalized Sc_2C MXenes. *Phys. Rev. B* **2016**, *94*, 035405.

[46] Lu, S.; Ren, W. J.; He, J.; Yu, C. Q.; Jiang, P. F.; Chen, J. Enhancement of the lattice thermal conductivity of two-dimensional functionalized MXenes by inversion symmetry breaking. *Phys. Rev. B* **2022**, *105*, 165301.

[47] Klemens, P. G.; Pedraza, D. F. Thermal conductivity of graphite in the basal plane. *Carbon* **1994**, *32*, 735–741.

[48] Klemens, P. G. Theory of thermal conduction in thin ceramic films. *Int. J. Thermophys.* **2001**, *22*, 265–275.

[49] Qian, X.; Zhou, J. W.; Chen, G. Phonon-engineered extreme thermal conductivity materials. *Nat. Mater.* **2021**, *20*, 1188–1202.

[50] Zha, X.-H.; Huang, Q.; He, J.; He, H. M.; Zhai, J. Y.; Francisco, J. S.; Du, S. Y. The thermal and electrical properties of the promising semiconductor MXene Hf_2CO_2. *Sci. Rep.* **2016**, *6*, 27971.

[51] Zha, X. H.; Yin, J. S.; Zhou, Y. H.; Huang, Q.; Luo, K.; Lang, J. J.; Francisco, J. S.; He, J.; Du, S. Y. Intrinsic structural, electrical, thermal, and mechanical properties of the promising conductor Mo_2C MXene. *J. Phys. Chem. C* **2016**, *120*, 15082–15088.

[52] Zha, X. H.; Zhou, J.; Zhou, Y. H.; Huang, Q.; He, J.; Francisco, J. S.; Luo, K.; Du, S. Y. Promising electron mobility and high thermal conductivity in Sc_2CT_2 (T = F, OH) MXenes. *Nanoscale* **2016**, *8*, 6110–6117.

[53] Gu, X. K.; Wei, Y. J.; Yin, X. B.; Li, B. W.; Yang, R. G. *Colloquium*: Phononic thermal properties of two-dimensional materials. *Rev. Mod. Phys.* **2018**, *90*, 041002.

[54] Shi, L. Nonresistive heat transport by collective phonon flow: "Second sound" has been observed in graphite. *Science* **2019**, *364*, 332–333.

[55] Lee, S.; Broido, D.; Esfarjani, K.; Chen, G. Hydrodynamic phonon transport in suspended graphene. *Nat. Commun.* **2015**, *6*, 6290.

[56] Cepellotti, A.; Fugallo, G.; Paulatto, L.; Lazzeri, M.; Mauri, F.; Marzari, N. Phonon hydrodynamics in two-dimensional materials. *Nat. Commun.* **2015**, *6*, 6400.

[57] Fermi, I.; Pasta, P.; Ulam, S.; Tsingou, M. Studies of the nonlinear problems: Los Alamos Scientific Lab. *N. Mex.*

[58] Chen, G. Thermal conductivity and ballistic-phonon transport in the cross-plane direction of superlattices. *Phys. Rev. B* **1998**, *57*, 14958–14973.

[59] Guo, Z. L.; Miao, N. H.; Zhou, J.; Pan, Y. C.; Sun, Z. M. Coincident modulation of lattice and electron thermal transport performance in MXenes via surface functionalization. *Phys. Chem. Chem. Phys.* **2018**, *20*, 19689–19697.

[60] Sarikurt, S.; Çakır, D.; Keçeli, M.; Sevik, C. The influence of surface functionalization on thermal transport and thermoelectric properties of MXene monolayers. *Nanoscale* **2018**, *10*, 8859–8868.

[61] Gholivand, H.; Fuladi, S.; Hemmat, Z.; Salehi-Khojin, A.; Khalili-Araghi, F. Effect of surface termination on the lattice thermal conductivity of monolayer $Ti_3C_2T_z$ MXenes. *J. Appl. Phys.* **2019**, *126*, 065101.

[62] Wang, A.; Li, S. H.; Zhang, X. Y.; Bao, H. Roles of electrons on the thermal transport of 2D metallic MXenes. *Phys. Rev. Mater.* **2022**, *6*, 014009.

[63] Wu, H.; Gu, J. X.; Li, Z. C.; Liu, W. X.; Bao, H.; Lin, H.; Yue, Y. A. Characterization of phonon thermal transport of $Ti_3C_2T_x$ MXene thin film. *J. Phys.: Condens. Matter* **2022**, *34*, 155704.

[64] Yu, L. T.; Huang, D. Z.; Wang, X. Z.; Yu, W.; Yue, Y. A. Tuning thermal and electrical properties of MXenes via dehydration. *Phys. Chem. Chem. Phys.* **2022**, *24*, 25969–25978.

[65] Chen, L.; Shi, X. G.; Yu, N. J.; Zhang, X.; Du, X. Z.; Lin, J. Measurement and analysis of thermal conductivity of $Ti_3C_2T_x$ MXene films. *Materials* **2018**, *11*, 1701.

[66] Liu, R.; Li, W. H. High-thermal-stability and high-thermal-conductivity $Ti_3C_2T_x$ MXene/poly(vinyl alcohol) (PVA) composites. *ACS Omega* **2018**, *3*, 2609–2617.

[67] Gandi, A. N.; Alshareef, H. N.; Schwingenschlögl, U. Thermoelectric performance of the MXenes M_2CO_2 (M = Ti, Zr, or

Hf). *Chem. Mater.* **2016**, *28*, 1647–1652.
[68] Rohsenow, W. M.; Hartnett, J. P.; Cho, Y. I. *Handbook of Heat Transfer*; 3rd ed. McGraw-Hill: New York, 1998.
[69] Kim, H.; Anasori, B.; Gogotsi, Y.; Alshareef, H. N. Thermoelectric properties of two-dimensional molybdenum-based MXenes. *Chem. Mater.* **2017**, *29*, 6472–6479.
[70] Lu, X. F.; Zhang, Q. H.; Liao, J. C.; Chen, H. Y.; Fan, Y. C.; Xing, J. J.; Gu, S. J.; Huang, J. L.; Ma, J. X.; Wang, J. C. et al. High-efficiency thermoelectric power generation enabled by homogeneous incorporation of MXene in $(Bi,Sb)_2Te_3$ matrix. *Adv. Energy Mater.* **2020**, *10*, 1902986.
[71] Schultz, T.; Frey, N. C.; Hantanasirisakul, K.; Park, S.; May, S. J.; Shenoy, V. B.; Gogotsi, Y.; Koch, N. Surface termination dependent work function and electronic properties of $Ti_3C_2T_x$ MXene. *Chem. Mater.* **2019**, *31*, 6590–6597.
[72] Persson, I.; Näslund, L. Å.; Halim, J.; Barsoum, M. W.; Darakchieva, V.; Palisaitis, J.; Rosen, J.; Persson, P. O. Å. On the organization and thermal behavior of functional groups on Ti_3C_2 MXene surfaces in vacuum. *2D Mater.* **2018**, *5*, 015002.
[73] Hart, J. L.; Hantanasirisakul, K.; Lang, A. C.; Anasori, B.; Pinto, D.; Pivak, Y.; van Omme, J. T.; May, S. J.; Gogotsi, Y.; Taheri, M. L. Control of MXenes' electronic properties through termination and intercalation. *Nat. Commun.* **2019**, *10*, 522.
[74] Fujii, M.; Zhang, X.; Xie, H. Q.; Ago, H.; Takahashi, K.; Ikuta, T.; Abe, H.; Shimizu, T. Measuring the thermal conductivity of a single carbon nanotube. *Phys. Rev. Lett.* **2005**, *95*, 065502.
[75] Wang, R. D.; Xu, S.; Yue, Y. A.; Wang, X. W. Thermal behavior of materials in laser-assisted extreme manufacturing: Raman-based novel characterization. *Int. J. Extrem. Manuf.* **2020**, *2*, 032004.
[76] Wang, R. D.; Hunter, N.; Zobeiri, H.; Xu, S.; Wang, X. W. Critical problems faced in Raman-based energy transport characterization of nanomaterials. *Phys. Chem. Chem. Phys.* **2022**, *24*, 22390–22404.
[77] Zobeiri, H.; Wang, R. D.; Deng, C.; Zhang, Q. Y.; Wang, X. W. Polarized Raman of nanoscale two-dimensional materials: Combined optical and structural effects. *J. Phys. Chem. C* **2019**, *123*, 23236–23245.
[78] Xu, S.; Fan, A.; Wang, H.; Zhang, X.; Wang, X. Raman-based nanoscale thermal transport characterization: A critical review. *Int. J. Heat Mass Transfer* **2020**, *154*, 119751.
[79] Li, C. Z.; Xu, S.; Yue, Y. A.; Yang, B.; Wang, X. W. Thermal characterization of carbon nanotube fiber by time-domain differential Raman. *Carbon* **2016**, *103*, 101–108.
[80] Wang, T. Y.; Xu, S.; Hurley, D. H.; Yue, Y. A.; Wang, X. W. Frequency-resolved Raman for transient thermal probing and thermal diffusivity measurement. *Opt. Lett.* **2016**, *41*, 80–83.
[81] Wang, T. Y.; Han, M.; Wang, R. D.; Yuan, P. Y.; Xu, S.; Wang, X. W. Characterization of anisotropic thermal conductivity of suspended nm-thick black phosphorus with frequency-resolved Raman spectroscopy. *J. Appl. Phys.* **2018**, *123*, 145104.
[82] Yuan, P. Y.; Wang, R. D.; Tan, H.; Wang, T. Y.; Wang, X. W. Energy transport state resolved Raman for probing interface energy transport and hot carrier diffusion in few-layered MoS_2. *ACS Photonics* **2017**, *4*, 3115–3129.
[83] Yuan, P. Y.; Tan, H.; Wang, R. D.; Wang, T. Y.; Wang, X. W. Very fast hot carrier diffusion in unconstrained MoS_2 on a glass substrate: Discovered by picosecond ET-Raman. *RSC Adv.* **2018**, *8*, 12767–12778.
[84] Zobeiri, H.; Wang, R. D.; Zhang, Q. Y.; Zhu, G. J.; Wang, X. W. Hot carrier transfer and phonon transport in suspended nm WS_2 films. *Acta Mater.* **2019**, *175*, 222–237.
[85] Zobeiri, H.; Hunter, N.; Wang, R. D.; Liu, X. M.; Tan, H.; Xu, S.; Wang, X. W. Thermal conductance between water and nm-thick WS_2: Extremely localized probing using nanosecond energy transport state-resolved Raman. *Nanoscale Adv.* **2020**, *2*, 5821–5832.
[86] Lin, H.; Wang, R. D.; Zobeiri, H.; Wang, T. Y.; Xu, S.; Wang, X. W. The in-plane structure domain size of nm-thick $MoSe_2$ uncovered by low-momentum phonon scattering. *Nanoscale* **2021**, *13*, 7723–7734.
[87] Zobeiri, H.; Wang, R. D.; Wang, T. Y.; Lin, H.; Deng, C.; Wang, X. W. Frequency-domain energy transport state-resolved Raman for measuring the thermal conductivity of suspended nm-thick $MoSe_2$. *Int. J. Heat Mass Transfer* **2019**, *133*, 1074–1085.
[88] Yao, J. R.; Zhou, J. T.; Yang, F.; Peng, G. Y.; Liu, Y. J.; Yao, Z. J.; Wu, F.; Zeng, H. B. Multi-functional and multi-scenario applications for MXene aerogels with synergistically enhanced asymmetric modules. *Nano Res.* **2024**, *17*, 3359–3368.
[89] Li, M. K.; Sun, Y. Y.; Feng, D. Y.; Ruan, K. P.; Liu, X.; Gu, J. W. Thermally conductive polyvinyl alcohol composite films via introducing hetero-structured MXene@silver fillers. *Nano Res.* **2023**, *16*, 7820–7828.
[90] Wang, J. E.; Song, T. L.; Ming, W.; Yele, M.; Chen, L. F.; Zhang, H.; Zhang, X. J.; Liang, B. L.; Wang, G. S. High MXene loading, nacre-inspired MXene/ANF electromagnetic interference shielding composite films with ultralong strain-to-failure and excellent Joule heating performance. *Nano Res.* **2024**, *17*, 2061–2069.
[91] Cao, Y.; Deng, Q. H.; Liu, Z. D.; Shen, D. Y.; Wang, T.; Huang, Q.; Du, S. Y.; Jiang, N.; Lin, C. T.; Yu, J. H. Enhanced thermal properties of poly(vinylidene fluoride) composites with ultrathin nanosheets of MXene. *RSC Adv.* **2017**, *7*, 20494–20501.
[92] Yan, C. Z.; Ji, C.; Zeng, X. L.; Sun, R.; Wong, C. P. Interconnecting the promising MXenes via Ag nanowire in epoxy nanocomposites for high-performance thermal management applications. In *Proceedings of the 2018 19th International Conference on Electronic Packaging Technology*, Shanghai, China, 2018; pp 510–512.
[93] Kang, R. Y.; Zhang, Z. Y.; Guo, L. C.; Cui, J. F.; Chen, Y. P.; Hou, X.; Wang, B.; Lin, C. T.; Jiang, N.; Yu, J. H. Enhanced thermal conductivity of epoxy composites filled with 2D transition metal carbides (MXenes) with ultralow loading. *Sci. Rep.* **2019**, *9*, 9135.
[94] Aakyiir, M.; Yu, H. M.; Araby, S.; Wang, R. Y.; Michelmore, A.; Meng, Q. S.; Losic, D.; Choudhury, N. R.; Ma, J. Electrically and thermally conductive elastomer by using MXene nanosheets with interface modification. *Chem. Eng. J.* **2020**, *397*, 125439.
[95] Chen, L.; Cao, Y.; Zhang, X.; Guo, X. B.; Song, P.; Chen, K.; Lin, J. Anisotropic and high thermal conductivity of epoxy composites containing multilayer $Ti_3C_2T_x$ MXene nanoflakes. *J. Mater. Sci.* **2020**, *55*, 16533–16543.
[96] Ji, C.; Wang, Y.; Ye, Z. Q.; Tan, L. Y.; Mao, D. S.; Zhao, W. G.; Zeng, X. L.; Yan, C. Z.; Sun, R.; Kang, D. J. et al. Ice-templated MXene/Ag-epoxy nanocomposites as high-performance thermal management materials. *ACS Appl. Mater. Interfaces* **2020**, *12*, 24298–24307.
[97] Jin, X. X.; Wang, J. F.; Dai, L. Z.; Liu, X. Y.; Li, L.; Yang, Y. Y.; Cao, Y. X.; Wang, W. J.; Wu, H.; Guo, S. Y. Flame-retardant poly(vinyl alcohol)/MXene multilayered films with outstanding electromagnetic interference shielding and thermal conductive performances. *Chem. Eng. J.* **2020**, *380*, 122475.
[98] Mazhar, S.; Qarni, A. A.; Ul Haq, Y.; Ul Haq, Z.; Murtaza, I. Promising PVC/MXene based flexible thin film nanocomposites with excellent dielectric, thermal and mechanical properties. *Ceram. Int.* **2020**, *46*, 12593–12605.
[99] Wang, D. Z.; Lin, Y.; Hu, D. W.; Jiang, P. K.; Huang, X. Y. Multifunctional 3D-MXene/PDMS nanocomposites for electrical, thermal and triboelectric applications. *Composites Part A* **2020**, *130*, 105754.
[100] Gao, Q. S.; Pan, Y. M.; Zheng, G. Q.; Liu, C. T.; Shen, C. Y.; Liu, X. H. Flexible multilayered MXene/thermoplastic polyurethane films with excellent electromagnetic interference shielding, thermal conductivity, and management performances. *Adv. Compos. Hybrid Mater.* **2021**, *4*, 274–285.
[101] Liu, L.; Ying, G. B.; Wen, D.; Zhang, K. C.; Hu, C.; Zheng, Y. T.; Zhang, C.; Wang, X.; Wang, C. Aqueous solution-processed MXene ($Ti_3C_2T_x$) for non-hydrophilic epoxy resin-based composites with enhanced mechanical and physical properties. *Mater. Des.* **2021**, *197*, 109276.
[102] Ma, S. F.; Zhu, S. L.; Liu, M. L.; Zhong, B. C.; Chen, Y. J.; Luo, Y. F.; Liu, F.; Jia, Z. X.; Jia, D. M. A high-performance, thermal and electrical conductive elastomer composite based on Ti_3C_2 MXene. *Composites Part A* **2021**, *145*, 106292.

[103] Wang, D. Z.; Wei, H.; Lin, Y.; Jiang, P. K.; Bao, H.; Huang, X. Y. Achieving ultrahigh thermal conductivity in Ag/MXene/epoxy nanocomposites via filler-filler interface engineering. *Compos. Sci. Technol.* **2021**, *213*, 108953.

[104] Zhan, Y. J.; Nan, B. F.; Liu, Y. C.; Jiao, E. X.; Shi, J.; Lu, M. G.; Wu, K. Multifunctional cellulose-based fireproof thermal conductive nanocomposite films assembled by *in-situ* grown SiO_2 nanoparticle onto MXene. *Chem. Eng. J.* **2021**, *421*, 129733.

[105] Jiao, E. X.; Wu, K.; Liu, Y. C.; Lu, M. P.; Hu, Z. R.; Chen, B.; Shi, J.; Lu, M. G. Ultrarobust MXene-based laminated paper with excellent thermal conductivity and flame retardancy. *Composites Part A* **2021**, *146*, 106417.

[106] Zhou, B.; Li, Q. T.; Xu, P. H.; Feng, Y. Z.; Ma, J. M.; Liu, C. T.; Shen, C. Y. An asymmetric sandwich structural cellulose-based film with self-supported MXene and AgNW layers for flexible electromagnetic interference shielding and thermal management. *Nanoscale* **2021**, *13*, 2378–2388.

[107] Liu, H. B.; Huang, Z. Y.; Chen, T.; Su, X. Q.; Liu, Y. N.; Fu, R. L. Construction of 3D MXene/Silver nanowires aerogels reinforced polymer composites for extraordinary electromagnetic interference shielding and thermal conductivity. *Chem. Eng. J.* **2022**, *427*, 131540.

[108] Liu, H. G.; Wang, Z.; Yang, Y. J.; Wu, S. Q.; Wang, C. K.; You, C. Y.; Tian, N. Thermally conductive MWCNTs/Fe_3O_4/$Ti_3C_2T_x$ MXene multi-layer films for broadband electromagnetic interference shielding. *J. Mater. Sci. Technol.* **2022**, *130*, 75–85.

[109] Qin, Y.; Li, L. H.; Li, M. H.; Wei, X. Z.; Xiong, S. Y.; Xia, J. C.; Kong, X. D.; Wang, Y. D.; Cai, T.; Deng, L. F. et al. Flexible MXene/copper/cellulose nanofiber heat spreader films with enhanced thermal conductivity. *Nanotechnol. Rev.* **2022**, *11*, 1583–1591.

[110] Yan, Y. Z.; Li, S. W.; Park, S. S.; Zhang, W. J.; Lee, J. S.; Kim, J. R.; Seong, D. G.; Ha, C. S. "One stone, two birds" solvent system to fabricate microcrystalline cellulose-$Ti_3C_2T_x$ nanocomposite film as a flexible dielectric and thermally conductive material. *Nano Res.* **2023**, *16*, 3240–3253.

[111] Huang, X.; Tuersun, Y.; Huang, M.; Lin, W.; Qiu, W.; Chu, S. Highly enhanced thermal conductivity from boron nitride nanosheets and MXene phonon resonance in 3D PMMA spheres composites. *Mater. Today Sustain.* **2023**, *21*, 100269.

[112] Lee, J.; Kim, J. Enhancing the thermal conductivity of PEG composites with freeze-drying and surface treatment of MXene and CNT. *Mater. Today Chem.* **2023**, *27*, 101305.

[113] Kong, X. D.; Song, G. C.; Chen, Y. P.; Chen, X. M.; Li, M. H.; Li, L. H.; Wang, Y. D.; Gong, P.; Zhang, Z. B.; Zhang, J. X. et al. Mannitol enhanced thermal conductivity and environmental stability of highly aligned MXene composite film. *Compos. Sci. Technol.* **2023**, *241*, 110141.

[114] Pietrak, K.; Wiśniewski, T. S. A review of models for effective thermal conductivity of composite materials. *J. Power Technol.* **2015**, *95*, 14–24.

[115] Foygel, M.; Morris, R. D.; Anez, D.; French, S.; Sobolev, V. L. Theoretical and computational studies of carbon nanotube composites and suspensions: Electrical and thermal conductivity. *Phys. Rev. B* **2005**, *71*, 104201.

[116] Bird, R. B. Transport phenomena. *Appl. Mech. Rev.* **2002**, *55*, R1–R4.

[117] Maxwell, J. C. *A Treatise on Electricity and Magnetism*; Clarendon Press: Oxford, 1873.

[118] Swartz, E. T.; Pohl, R. O. Thermal boundary resistance. *Rev. Mod. Phys.* **1989**, *61*, 605–668.

[119] Ruan, K.; Shi, X.; Guo, Y.; Gu, J. Interfacial thermal resistance in thermally conductive polymer composites: A review. *Compos. Commun.* **2020**, *22*, 100518.

[120] Hasselman, D. P. H.; Johnson, L. F. Effective thermal conductivity of composites with interfacial thermal barrier resistance. *J. Compos. Mater.* **1987**, *21*, 508–515.

[121] Nan, C. W.; Birringer, R.; Clarke, D. R.; Gleiter, H. Effective thermal conductivity of particulate composites with interfacial thermal resistance. *J. Appl. Phys.* **1997**, *81*, 6692–6699.

[122] Burger, N.; Laachachi, A.; Ferriol, M.; Lutz, M.; Toniazzo, V.; Ruch, D. Review of thermal conductivity in composites: Mechanisms, parameters and theory. *Prog. Polym. Sci.* **2016**, *61*, 1–28.

[123] He, Y. J.; Shao, Y. W.; Xiao, Y. Y.; Yang, J. H.; Qi, X. D.; Wang, Y. Multifunctional phase change composites based on elastic mxene/silver nanowire sponges for excellent thermal/solar/electric energy storage, shape memory, and adjustable electromagnetic interference shielding functions. *ACS Appl. Mater. Interfaces* **2022**, *14*, 6057–6070.